New constraints on the relationship between ^{26}Al and oxygen, calcium, and titanium isotopic variation in the early Solar System from a multielement isotopic study of spinel-hibonite inclusions

Levke Kööp [a,b,c,*], Daisuke Nakashima [d,e], Philipp R. Heck [a,b,c], Noriko T. Kita [d], Travis J. Tenner [d,i], Alexander N. Krot [f], Kazuhide Nagashima [f], Changkun Park [f,g], Andrew M. Davis [a,b,c,h]

[a] *Department of the Geophysical Sciences, The University of Chicago, Chicago, IL 60637, USA*
[b] *Chicago Center for Cosmochemistry, The University of Chicago, Chicago, IL 60637, USA*
[c] *Robert A. Pritzker Center for Meteoritics and Polar Studies, Field Museum of Natural History, Chicago, IL, USA*
[d] *Department of Geoscience, University of Wisconsin, Madison, WI 53706, USA*
[e] *Division of Earth and Planetary Material Sciences, Faculty of Science, Tohoku University, Aoba, Sendai, Miyagi 980-8578, Japan*
[f] *Hawai'i Institute of Geophysics and Planetology, School of Ocean and Earth Science and Technology, University of Hawai'i at Mānoa, Honolulu, HI, USA*
[g] *Korea Polar Research Institute, Incheon 406-840, Republic of Korea*
[h] *Enrico Fermi Institute, The University of Chicago, Chicago, IL 60637, USA*
[i] *Chemistry Division, Nuclear and Radiochemistry, Los Alamos National Laboratory, MSJ514, Los Alamos, NM 87545, USA*

Received 21 September 2015; accepted in revised form 9 April 2016; available online 20 April 2016

Abstract

We report oxygen, calcium, titanium and ^{26}Al–^{26}Mg isotope systematics for spinel-hibonite inclusions (SHIBs), a class of calcium–aluminum-rich inclusions (CAI) common in CM chondrites. In contrast to previous studies, our analyses of 33 SHIBs and four SHIB-related objects obtained with high spatial resolution demonstrate that these CAIs have a uniform Δ^{17}O value of approximately −23‰, similar to many other mineralogically pristine CAIs from unmetamorphosed chondrites (e.g., CR, CV, and Acfer 094). Five SHIBs studied for calcium and titanium isotopes have no resolvable anomalies beyond 3σ uncertainties. This suggests that nucleosynthetic anomalies in the refractory elements had been significantly diluted in the environment where SHIBs with uniform Δ^{17}O formed. We established internal ^{26}Al–^{26}Mg isochrons for eight SHIBs and found that seven of these formed with uniformly high levels of ^{26}Al (a multi-CAI mineral isochron yields an initial ^{26}Al/^{27}Al ratio of ~4.8×10^{-5}), but one SHIB has a smaller initial ^{26}Al/^{27}Al of ~2.5×10^{-5}, indicating variation in ^{26}Al/^{27}Al ratios when SHIBs formed. The uniform calcium, titanium and oxygen isotopic characteristics found in SHIBs with both high and low initial ^{26}Al/^{27}Al ratios allow for two interpretations. (1) If subcanonical initial ^{26}Al/^{27}Al ratios in SHIBs are due to early formation, as suggested by Liu et al. (2012), our data would indicate that the CAI formation region had achieved a high degree of isotopic homogeneity in oxygen and refractory elements before a homogeneous distribution of ^{26}Al was achieved. (2) Alternatively, if subcanonical ratios were the result of ^{26}Al–^{26}Mg system resetting, the clustering of SHIBs at a Δ^{17}O value of ~−23‰ would imply that a ^{16}O-rich gaseous reservoir existed in the nebula until at least ~0.7 Ma after the formation of the majority of CAIs.

© 2016 Elsevier Ltd. All rights reserved.

* Corresponding author at: Department of the Geophysical Sciences, The University of Chicago, Chicago, IL 60637, USA.
E-mail address: koeoep@uchicago.edu (L. Kööp).

1. INTRODUCTION

Calcium-, aluminum-rich inclusions (CAIs) are the oldest dated objects that formed in the Solar System (Amelin et al., 2002; Connelly et al., 2012). Preserved within and delivered by primitive meteorites, CAIs provide a wealth of information about processes that occurred in the early Solar System, as well as the nature of the material that the Solar System originated from. For instance, resolvable mass-independent isotopic anomalies of CAIs can be linked to predicted nucleosynthetic signatures of evolved stars (e.g., Trinquier et al., 2009). Another example is that many CAIs attest to the presence of short-lived radionuclides (SLRs) like ^{26}Al in the early Solar System (e.g., Lee et al., 1976). Most isotopic studies of CAIs have been focused on the sizable examples found in CV chondrites, which promote the view that CAIs formed when ^{26}Al was at a high and uniform abundance in the solar nebula (canonical level of $\sim 5.2 \times 10^{-5}$; Jacobsen et al., 2008; MacPherson et al., 2012). However, with advancements in the analysis of smaller samples, an increasing number of CAIs from other chondrite groups has been studied. They show that many CAIs formed with lower than canonical levels of ^{26}Al (e.g., depletions of up to $\sim 50\%$ of the canonical ratio are common) or even without ^{26}Al (Krot et al., 2012, and references therein). Often, subcanonical levels of ^{26}Al are interpreted as formation or reprocessing after significant decay of ^{26}Al (e.g., for CV CAIs with ratios between 5.17×10^{-5} and 2.77×10^{-5}; MacPherson et al., 2012). However, compelling arguments have been made that a significant number of CAIs formed earlier than canonical CV CAIs, in spite of showing no evidence for incorporation of live ^{26}Al or having formed with subcanonical levels of ^{26}Al (e.g., $\sim (5.2 \pm 1.7) \times 10^{-8}$ for HAL; Fahey et al., 1987; Wood, 1998; Sahijpal and Goswami, 1998). Among these are the enigmatic FUN (fractionated and unidentified nuclear effects; e.g., Wasserburg et al., 1977) CAIs and the PLACs (platy hibonite crystals; e.g., Ireland, 1990). The large magnitudes of nucleosynthetic anomalies in these CAIs attest to their formation at an early stage of Solar System evolution, which was characterized by large isotopic heterogeneities. The lack of evidence for the initial presence of ^{26}Al among these CAIs suggests that this SLR was initially absent in the CAI formation region and was introduced at a later stage, possibly due to a late injection from a nearby star (Wood, 1998; Sahijpal and Goswami, 1998).

Most studies of PLACs also present data for the spinel-hibonite inclusions (SHIBs), likely because both types of CAIs are abundant in CM chondrites, contain hibonite, and are recovered using the same analytical protocols (MacPherson et al., 1980). In contrast to the ^{26}Al-free PLACs, SHIBs have variable inferred $^{26}Al/^{27}Al$ ratios ranging from zero to supracanonical, which could indicate that

they formed while ^{26}Al was admixed into the Solar System (e.g., Liu et al., 2012). This interpretation is strengthened by the magnitude of nucleosynthetic anomalies in SHIBs, which are intermediate between the ^{26}Al-depleted PLACs and regular CAIs with canonical initial abundances of ^{26}Al (e.g., $\delta^{50}Ti$ ranges of $>300‰$ in PLACs, mostly within $\pm 10‰$ for SHIBs and up to $\sim 1‰$ in CV CAIs; Ireland, 1988, 1990; Sahijpal et al., 2000; Liu et al., 2009a; Trinquier et al., 2009). If true, this would make SHIBs key samples for understanding the processes that governed admixture of ^{26}Al and dilution of nucleosynthetic anomalies in the early Solar System. However, it remains unclear how the oxygen isotopes of SHIBs and PLACs fit into this picture. Many primitive CAIs have a $\Delta^{17}O \sim -23‰$, with minor variations between $\sim -25‰$ and $-21‰$ (e.g., CAIs from Acfer 094, CR chondrites, certain primary phases in CV CAIs and Wark-Lovering rims; Makide et al., 2009; Ushikubo et al., 2011; Bullock et al., 2012; Bodénan et al., 2014), suggesting they formed in a fairly uniform oxygen isotopic reservoir. In contrast, SHIBs and PLACs have been reported to be more variable in $\Delta^{17}O$, ranging from approximately $-28‰$ to $-15‰$ (Liu et al., 2009a). Analogous to the larger degree of isotopic heterogeneity in calcium and titanium, SHIBs and PLACs appear to indicate that the solar nebula was also initially isotopically heterogeneous in oxygen. After formation of PLACs and SHIBs, this heterogeneity may have been erased by mixing and/or thermal processes, allowing formation of CAIs with largely uniform oxygen isotopic compositions. However, other studies report more variable $\Delta^{17}O$ values for CAIs and related materials (e.g., Itoh and Yurimoto, 2003; Simon et al., 2011; Park et al., 2012) and interpret the results in favor of coexistence and exchange between ^{16}O-poor and ^{16}O-rich reservoirs while CAIs formed. If true, this interpretation could also account for the reported oxygen isotopic variations in SHIBs and PLACs.

An issue with previous studies of SHIBs is that they were usually limited to a single spot analysis per CAI by secondary ion mass spectrometry (SIMS). This is particularly problematic for obtaining accurate initial $^{26}Al/^{27}Al$ ratios as well as oxygen isotope data in these samples. For example, $^{26}Al/^{27}Al$ ratios are usually inferred from model isochrons constructed from a single spot analysis (commonly referred to as bulk analysis) and an assumed initial magnesium isotopic composition for an intercept (i.e., terrestrial). Possible problems include (1) variations in the initial magnesium isotopic composition, (2) resetting (partial or complete; e.g., Simon and Young, 2011; MacPherson et al., 2012), and (3) contributions from alteration phases. As studies of PLACs indicate (e.g., Liu et al., 2009a), the assumption of isotopically uniform magnesium is not trivial for early Solar System materials, particularly if SHIBs formed early (e.g., Liu et al., 2012). As such, variations in the initial magnesium isotopic compositions translate

directly into incorrect values for inferred $^{26}Al/^{27}Al$. Internal disturbance is a relevant complication (Liu et al., 2009b). If SIMS analyses do not sample internally disturbed SHIBs representatively (not a true bulk), the measured compositions will be offset from the bulk isochron, which leads to erroneous model $^{26}Al/^{27}Al$ ratios. Similarly, sampling of alteration phases, which commonly occur in cracks and voids in SHIBs, could also move data off the proper isochron. Finally, contributions from ^{16}O-poor alteration phases could introduce artificial variation in oxygen-isotope measurements of SHIBs.

Here, we report results from a multielement isotopic study of SHIBs in which we emphasized avoiding potential sources of contamination. Our objective is to further evaluate if SHIBs record the admixing of ^{26}Al into the CAI formation region, and to determine the degree of isotopic homogeneity in the SHIB-forming reservoir. We analyzed the magnesium isotopic composition in both spinel and hibonite grains within individual SHIBs with high-spatial-resolution using the WiscSIMS Cameca IMS 1280 (Kita et al., 2012), which allowed us to infer initial $^{26}Al/^{27}Al$ ratios from internal isochrons while avoiding the problems summarized above. In addition, we reinvestigated the oxygen isotopic systematics in a large number of SHIBs with the WiscSIMS instrument, with a spatial resolution that allowed us to avoid sampling of alteration phases. Finally, we obtained calcium and titanium isotopic data for a subset of the SHIBs using the Cameca IMS 1280 at the University of Hawai'i, in order to investigate relationships between the abundance of ^{26}Al and the magnitude of nucleosynthetic anomalies.

2. METHODS

2.1. Sample recovery and selection

SHIBs were separated from the Murchison CM2 chondrite along with other hibonite-rich CAIs (e.g., PLACs described in Kööp et al., 2014a, 2015). Part of the sample set was picked from an existing Murchison HF-HCl acid residue (Amari et al., 1994); other samples were recovered from the dense fraction of a freshly disaggregated Murchison rock fragment (not acid-treated, approximately 92 g from Field Museum specimen ME 2644). All CAIs investigated were mounted on conductive tape for preliminary classification by scanning electron microscopy (SEM). Almost all samples studied here contain spinel and hibonite; exceptions are three xenomorphic hibonite grains that are likely fragments of SHIBs (see Section 3.1). Samples were selected to include both the most abundant types of SHIBs as well as spinel-hibonite-rich CAIs with unusual morphology or mineralogy (including a melilite-bearing spinel-hibonite inclusion), and all SHIBs deemed suitable for the $^{26}Al–^{26}Mg$ and calcium–titanium isotope study.

2.2. Sample preparation

After initial characterization, the samples were removed from the conductive tape and cleaned with high purity iso-propanol (Fisher Optima™ grade). After drying, they were mounted in the center of one-inch epoxy disks together with terrestrial mineral standards. A total of 19 epoxy mounts were prepared, which contain between one and 14 CAIs each. The samples presented here are located in 10 different mounts. The mounts were polished using a combination of lapping films and polishing pads to prepare sufficiently flat surfaces to avoid problems with instrumental mass fractionation due to sample topography (Kita et al., 2009). For nine randomly selected mounts, we checked the polishing relief with a Zygo profilometer at the University of Wisconsin, which showed that height differences between grains and epoxy were ⩽2 μm, and the typical profile over a one-inch disk surface was ⩽10 μm. The polished mounts were carbon-coated for elemental and isotopic analyses.

2.3. Electron microscopy

The CAIs were characterized with a Zeiss EVO 60 SEM at the Field Museum, a JEOL JSM-5800LV SEM, and a TESCAN LYRA3 SEM/FIB at the University of Chicago, all equipped with Oxford Instruments energy dispersive spectroscopy (EDS) systems. The samples were analyzed by EDS and imaged in backscattered electrons (BSE) and secondary electrons both prior to and after polishing. The data were then used for identifying the most suitable locations for isotope analysis. Quantitative EDS analyses were obtained for spinel grains using an Oxford XMax SDD EDS detector, operating Oxford AZtec software, on the TESCAN LYRA3, using a 15 kV acceleration voltage at a deadtime of ∼56%. An energy calibration and a beam intensity measurement were performed on cobalt metal prior to spinel analyses. A microprobe spinel standard of known composition (by weight: 0.1709% Mg, 0.3793% Al and 0.4498% O) and a Burma spinel standard were analyzed alongside spinel grains in SHIBs. Oxygen was quantified by stoichiometry and the data was normalized to a sum of 100%. EDS elemental maps of SHIBs were also collected with the TESCAN LYRA3, the data were normalized to a sum of 100%. The associated uncertainty of the maps is on the order of 5%.

2.4. Electron microprobe analysis

Hibonite grains in the CAIs were analyzed with a Cameca SX-50 electron probe microanalyzer (EPMA) at the University of Chicago. Most grains were analyzed with a 50 nA beam and an acceleration voltage of 15 kV; for a small subset, a higher beam current and acceleration voltage was used (100 nA and 20 kV). For standardization, we used manganese hortonolite for magnesium and iron, corundum for aluminum, and anorthite for calcium. The analyses of the corundum standards yielded negative apparent abundances for magnesium, which is a result of the curvature in the background signal caused by the high aluminum signal. We corrected unknown analyses for the curved background using data from multiple peak scans on a corundum standard. The effect of this correction is negligible for all except the most magnesium-depleted hibonite measurement in CAI 1-10-5.

2.5. Isotopic analyses

2.5.1. Oxygen

The CAIs were measured for their oxygen isotopic composition with the WiscSIMS Cameca IMS 1280 (Kita et al., 2009, 2010) with conditions similar to those described by Nakashima et al. (2011). The three isotopes of oxygen were simultaneously detected using a Faraday cup (FC) for $^{16}O^-$ and electron multipliers (EM) for $^{17}O^-$ and $^{18}O^-$. Two to four spots were analyzed in every CAI. A San Carlos olivine standard was analyzed and used for bracketing of unknown analyses (running standard) and appropriate WiscSIMS mineral standards (Heck et al. 2010; Kita et al. 2012) were used to correct for the instrumental bias affecting the different analyzed phases (hibonite, spinel and gehlenite). The external reproducibility of eight bracketing standard measurements was ~0.5–1.6‰ (2 standard deviations, SD) for $\delta^{18}O$, $\delta^{17}O$, and $\Delta^{17}O$ and was assigned as analytical uncertainty of unknown samples in each bracket of 7 to 13 unknown analyses (see Kita et al., 2009, 2010 for details on data treatment). While the interference from the tail of the $^{16}OH^-$ peak on the $^{17}O^-$ signal was negligibly small ($\leqslant$0.5‰), the correction described by Heck et al. (2010) was applied. A small primary Cs^+ beam (~20 pA, ~3 × 4 μm^2) was chosen to allow analysis of individual primary minerals in the fine-grained samples. To confirm that adjacent primary and secondary minerals did not contribute to analyses, the analyzed areas were carefully examined by SEM. If a SIMS pit contained visible epoxy or included additional primary or secondary phases, the corresponding analysis was rejected (only 2 out of a total of 100 spot analyses had to be rejected). For all samples, oxygen was the first element studied for its isotopic composition to avoid problems with implantation of $^{16}O^-$, which was used as primary beam for the measurement of magnesium, calcium and titanium isotopes.

2.5.2. Aluminum–magnesium

Aluminum and magnesium isotopes were analyzed with the WiscSIMS Cameca IMS 1280. For hibonite grains, a 30–60 pA primary beam was focused to a diameter of ~5 μm and secondary magnesium isotopes were analyzed by monocollection EM detection, which was combined with an additional multicollector FC to allow for simultaneous detection of $^{27}Al^+$ with $^{25}Mg^+$ (Kita et al., 2012; Ushikubo et al., 2013). Entrance and exit slits used were 90 μm and 405 μm, respectively, and field and contrast apertures used were 4000 μm and 400 μm, respectively. The magnification of the transfer optics was set to 200 between the sample and the field aperture. The secondary $^{24}Mg^+$ signals were within a range of (0.3–1.7) × 10^5 cps for unknowns and (1.1–2.2) × 10^5 cps for the Madagascar hibonite standard. The Madagascar hibonite standard was analyzed to correct for the instrumental mass fractionation in unknown hibonites and to determine the relative sensitivity factor (RSF) between $^{27}Al^+$ and $^{24}Mg^+$ signals. A total of 100 to 200 cycles were acquired for each magnesium-isotope analysis, with counting times of 3 s for $^{24}Mg^+$ and 10 s for $^{25}Mg^+$, $^{26}Mg^+$, and $^{27}Al^+$ for each cycle. For unknowns, $\delta^{25}Mg$ and $\delta^{26}Mg$ values were calculated relative to standard measurements with the same number of cycles. The resulting uncertainties for $\delta^{26}Mg^*$ are 1.3–2.0‰ and 1.1–2.4‰ for 100- and 200-cycle measurements, respectively, and for both $\delta^{25}Mg$ and $\delta^{26}Mg$, uncertainties are 0.6–1.0‰ and 0.5–1.2‰ for 100- and 200-cycle analyses, respectively.

Spinel grains were analyzed by simultaneous detection of magnesium isotopes and ^{27}Al using four FCs with analytical conditions similar to those of olivine in chondrules by Ushikubo et al. (2013). A 2.13–2.18 nA primary O$^-$ beam was focused to a ~13 μm diameter, which yielded secondary $^{24}Mg^+$ signals within a range of (7.2–8.0) × 10^7 cps for unknowns and within (7.0–7.4) × 10^7 cps for the WiscSIMS spinel standard. Spinel standard analyses were used to determine the RSF between $^{27}Al^+$ and $^{24}Mg^+$ signals and to correct for the instrumental mass fractionation in unknown spinel grains (Kita et al., 2012). Counting times of individual ions for each cycle were 10 s for all isotopes ($^{24}Mg^+$, $^{25}Mg^+$, $^{26}Mg^+$, and $^{27}Al^+$), the total number of cycles for each magnesium-isotope analysis was 30, the resulting uncertainties are 0.1–0.2‰ for $\delta^{26}Mg^*$ and $\delta^{25}Mg$, and 0.2–0.3‰ for $\delta^{26}Mg$.

For both hibonite and spinel standards, the absolute magnesium isotopic compositions are not known and assumed to be $\delta^{25}Mg_{DSM3} = 0$ (using the magnesium composition by Catanzaro et al., 1966). For the spinel standard, $\delta^{25}Mg$ and $\delta^{26}Mg^*$ are not expected to deviate from 0 by more than 1‰ and 0.1‰, respectively, based on the consistency of spinel, melilite, and fassaite data of Leoville CAIs (Kita et al., 2012) that were analyzed using the same spinel standard as well as melilite and fassaite standards with known magnesium isotope ratios. This is consistent with arguments for a high degree of homogeneity for terrestrial high-temperature minerals (e.g., Luu et al., 2013). Therefore, we expect that any associated potential bias is $\leqslant$1‰ in $\delta^{25}Mg$, and that any potential bias would not affect $\delta^{26}Mg^*$ values outside of the uncertainties of our measurements.

Excess ^{26}Mg was calculated using the relationship $\delta^{26}Mg^* = \delta^{26}Mg - [(1 + \delta^{25}Mg/1000)^{1/\beta} - 1] \times 1000$ (Kita et al., 2012). We used the updated β value of 0.5128 (Davis et al., 2015); however, no difference outside of quoted uncertainties is observed when the previously recommended β value of 0.514 (Davis et al., 2005) is applied. As indicated above, measured $^{27}Al/^{24}Mg$ ratios were corrected with the RSF obtained from standard measurements using the relationship $(^{27}Al/^{24}Mg)_{true} = (^{27}Al/^{24}Mg)_{SIMS}$ / RSF; the true ratios were obtained from EPMA analyses of the standard minerals and SIMS denotes the uncorrected, measured ratio. Isochrons were constructed using orthogonal distance regression (ODR; equivalent to a model 1 fit in Isoplot; Ludwig, 2003). The mean square weighted deviates (MSWD) were obtained with Isoplot (note that isochron slopes and intercepts are identical for ODR and Isoplot regression, but ODR uncertainties are slightly larger (difference in uncertainty estimates is usually <5%, but up to 24% in 1-3-1). Listed uncertainties on inferred $^{26}Al/^{27}Al$ ratios and intercepts ($\delta^{26}Mg_0^*$) are 2SD. As indicated above, Madagascar hibonite was used to obtain the RSF for hibonite analyses, which is similar to

previous studies (Ireland, 1988; Liu et al., 2012), but due to the standard's different mineral chemistry (higher FeO and REE content than in unknowns), the standard and unknowns could have different RSF values due to the matrix effect. In the Appendix, we also estimate an RSF from unknown EPMA analyses and discuss the effect on the slope of isochrons.

2.5.3. Calcium and titanium

A limited number of SHIBs were analyzed for calcium and titanium isotopes using a protocol similar to Park et al. (2014), which is based on previous studies of hibonite-rich CAIs (Fahey et al., 1987; Ireland, 1990). Using the Cameca IMS 1280 at the University of Hawai'i, the samples were analyzed with a primary O^- beam that was focused to a diameter of ~18 μm and set to ~0.6 nA prior to every analysis, but typically decreased by ~0.1 nA during the course of the analyses. The entrance and exit slits were at 31 μm and 94 μm, respectively, contrast and field apertures were at 400 μm and 3000 μm, respectively. The magnification of the transfer optics was ~160. $^{40}Ca^+$ was detected by FC, while the heavier calcium isotopes, all titanium isotopes and $^{51}V^+$, $^{52}Cr^+$, $^{53}Cr^+$ and $^{87}Sr^{2+}$ were sequentially detected by monocollection EM. The secondary $^{40}Ca^+$ signals were $(1.7–1.9) \times 10^6$ cps, signals for the other calcium and titanium isotopes measured by EM were between 2×10^3 and 2×10^5 cps. The detection efficiency of FC relative to the EM was determined from standard measurements so that the measured $^{40}Ca/^{44}Ca$ ratio plots on a linear mass fractionation line defined by other calcium isotope ratios determined by EM ($^{42}Ca/^{44}Ca$, $^{43}Ca/^{44}Ca$, and $^{48}Ca/^{44}Ca$). The resulting FC yield was 1.011 ± 0.029 (2σ). To correct for this efficiency difference, ^{40}Ca signals were divided by the FC yield. The EM dead-time was determined from TiO_2 standard analyses (28.9 ± 2.1 ns) and was corrected for using a method similar to those described by Fahey et al. (1987) and Fahey (1998). 60 cycles were acquired for each analysis of unknowns and standards, with individual counting times of 2 s for ^{40}Ca, ^{44}Ca, and ^{48}Ti, 4 s for ^{42}Ca, 4.96 s for $^{46}Ti^+$, $^{47}Ti^+$, $^{48}Ca^+$, $^{49}Ti^+$, $^{50}Ti^+$, $^{51}V^+$, $^{52}Cr^+$, and $^{53}Cr^+$, and 10 s for $^{43}Ca^+$.

A mass resolving power of ~11,170 was chosen to resolve the ^{48}Ca from the ^{48}Ti peak. However, the interference from $^{46}Ca^+$ on $^{46}Ti^+$ cannot be resolved at this mass resolution power and was corrected by assuming a terrestrial $^{46}Ca/^{44}Ca$ ratio for unknowns and standards. $^{51}V^+$, $^{52}Cr^+$ and $^{53}Cr^+$ were monitored to correct for potential isobaric interferences from $^{50}Cr^+$ and $^{50}V^+$ on $^{50}Ti^+$; $^{87}Sr^{2+}$ was monitored to assess potential interference from $^{88}Sr^{2+}$ on $^{44}Ca^+$. The contributions from $^{50}Cr^+$ and $^{50}V^+$ were calculated from measured ^{52}Cr and ^{51}V assuming terrestrial $^{50}Cr/^{52}Cr$ and $^{50}V/^{51}V$ ratios and corrected for, but are mostly insignificant ($\leqslant 0.3‰$ for $^{50}Cr^+$ and $^{50}V^+$) compared to analytical uncertainties. The contribution of $^{88}Sr^{2+}$ to $^{44}Ca^+$ is 0.1 ppm or less for the studied CAIs, which is negligible and no correction was applied. Instrumental fractionation was corrected for by sample-standard bracketing using three standard measurements collected on the same day as unknowns. The calcium and

titanium isotopic composition of the bracketing standard is assumed to correspond to the values listed in Niederer and Papanastassiou (1984) and Niederer et al. (1981), respectively. Any remaining mass-dependent fractionation was then corrected for under the assumption that it reflects the true mass-dependent fractionation within the sample (intrinsic fractionation; F_{Ca} and F_{Ti}) and that these elements evaporated or condensed as Ca atoms and TiO_2 molecules following a Rayleigh law, as recommended by Zhang et al. (2014). For calcium, ^{40}Ca and ^{44}Ca were used for normalization, while both the $^{49}Ti/^{47}Ti$ and $^{46}Ti/^{48}Ti$ pairs are considered for normalization of titanium isotopes. For all SHIBs, the targeted mineral was hibonite, but adjacent grains and cavities could not be avoided for some SHIBs (i.e., sparsely distributed sub-μm perovskite inclusions in 1-3-4, an adjacent spinel grain for 1-3-9, a cavity at edge of SIMS pit for 1-5-4), but post-SIMS SEM work showed no evidence that alteration phases contributed to the calcium and titanium analyses. Contribution from other primary minerals or surface topography could have resulted in a potential bias in our estimates for the mass-dependent fractionation intrinsic to these samples (F_{Ca} and F_{Ti}), but should not have resulted in a bias of the magnitude of isotope anomalies outside of the uncertainties achieved in this study.

3. RESULTS

3.1. Petrologic characteristics

The studied spinel-hibonite CAIs are ~30 μm to ~160 μm in their longest dimension and most resemble SHIBs described by previous authors (Ireland, 1988; Liu et al., 2009a). Accordingly, spinel and hibonite are the most abundant minerals in most of these CAIs. The relative abundances and grain sizes are highly variable, and both spinel and hibonite are usually more idiomorphic in coarse-grained SHIBs than in fine-grained examples (e.g., compare 1-2-1 and 1-10-5 with 1-6-6 in Fig. 1). Trace phases are common in many SHIBs, with perovskite being the most abundant, followed by FeO-poor silicates (usually clinopyroxene) and refractory metal nuggets (RMNs), but are entirely missing in some SHIBs. Voids and cracks are also common in both acid-treated and untreated SHIBs; in the latter, they are often filled with alteration phases (e.g., 1-5-4 and 1-3-1 in Fig. 1). Many untreated SHIBs preserve partial rims of secondary and sometimes primary silicates (Fig. 1c). Three irregularly shaped, spinel-free hibonite crystals were included in this study (Fig. 1b). All three have abundant holes and contain perovskite inclusions.

3.1.1. Mineral chemistry

Measured MgO and TiO_2 contents in SHIB hibonites range from 0.3 to 4.5 wt% and 0.2 to 10.7 wt%, respectively (Table 1). MgO and TiO_2 contents are generally correlated, as expected for the coupled substitution of $Mg^{2+} + Ti^{4+}$ for two Al^{3+} in hibonite (Fig. 2). FeO contents are usually below detection limit in SHIB hibonites (limits are 0.08 wt% for 20 kV and 0.03 wt% for 15 kV analyses). The few SHIB hibonite grains with FeO contents above detection
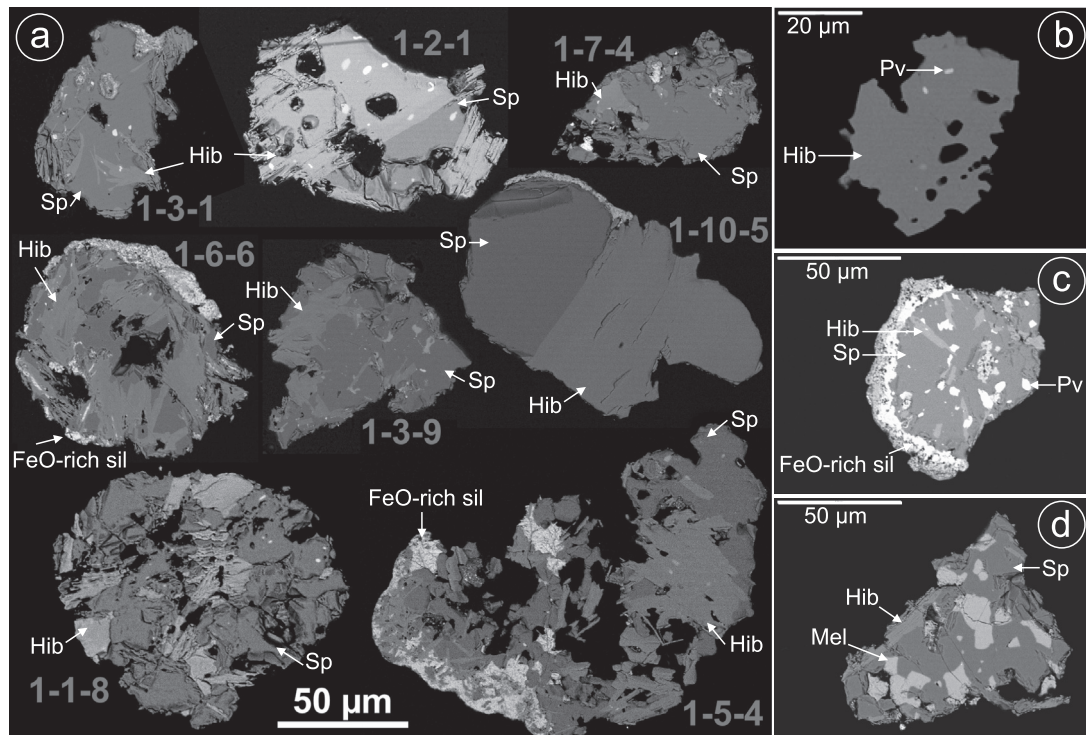
Fig. 1. BSE images of spinel-hibonite-rich CAIs. (a) Composite image of all eight SHIBs studied for ^{26}Al–^{26}Mg displayed at the same scale. (b) An irregularly shaped hibonite grain (2-2-3) with abundant rounded voids and perovskite inclusions that could have broken off a SHIB. (c) A fragment of a rounded SHIB (1-1-6) with radially oriented hibonite grains set in a dense spinel matrix. The inclusion is surrounded by a partial rim of Fe-rich alteration phases, followed by a layer of diopside. (d) A melilite-bearing spinel-hibonite inclusion (1-6-7). *Abbreviations:* Hib – hibonite, Pv – perovskite, Sp – spinel, Mel – melilite, FeO-rich sil – FeO-rich silicate.

limits are located in non-acid-treated SHIBs that preserve FeO-rich alteration phases (with one exception: no FeO-rich phases were observed in SHIB 1-1-3). EDS maps (Fig. 2) and EPMA analyses collected in different locations in the same hibonite crystals (Table 1) show that SHIB hibonites tend to be highly zoned in MgO and TiO$_2$.

The three irregularly shaped, spinel-free hibonite crystals have MgO and TiO$_2$ contents similar to hibonites and SHIBs (Table 1), and are distinctly enriched in these elements compared to PLAC-like CAIs studied in the same session (Kööp et al., 2014a).

Spinel grains were analyzed in six SHIBs (1-2-1, 1-3-1, 1-3-9, 1-5-4, 1-6-6, 1-10-5) as well as in the melilite–hibonite–spinel CAI 1-6-7. For all except 1-10-5, the analyses show minimal variations and yield compositions close to the stoichiometric MgAl$_2$O$_4$ endmember (Table 2; see Electronic appendix EA.1 for a full list of individual analyses). For 1-10-5, the analyses suggest excess Al$_2$O$_3$ in the spinel (nonstoichiometric spinel, approximately Mg$_{0.94}$Al$_{2.04}$O$_4$ if only Mg and Al are included in the quantification, or Mg$_{0.93}$Al$_{2.02}$V$_{0.02}$O$_4$ if other elements are included; Table 2). The analyses of the EPMA spinel standard ($N = 12$) deviate by less than 1% from the known composition (Section 2.3; Electronic appendix EA.1).

3.1.2. SHIBs studied for ^{26}Al–^{26}Mg

While many SHIBs contain either hibonite or spinel grains that are sufficiently large for magnesium isotope analyses (required sizes of ∼5 μm and ∼13 μm for hibonite

and spinel, respectively), after mounting in epoxy and polishing, only eight SHIBs had exposed grains of both minerals that were large enough for analysis. Of these SHIBs, three have rounded outer shapes consistent with (partial) melting (1-6-6, 1-1-8, 1-5-4); the other five have irregular shapes and could be fragments of larger inclusions (1-3-1, 1-2-1, 1-7-4, 1-3-9, 1-10-5). The rounded CAIs as well as 1-3-1 and 1-3-9 consist of multiple intergrown grains of spinel and hibonite with irregular boundaries, while 1-10-5, 1-2-1 and 1-7-4 appear to be dominated by more massive grains of spinel and/or hibonite with well-defined, linear grain boundaries. Trace phases (often perovskite, sometimes FeO-poor silicates) are present in all of these SHIBs except 1-10-5; non-acid treated samples 1-6-6, 1-3-1, 1-5-4 and 1-10-5 preserve partial rims of FeO-rich silicates. Similar FeO-rich material can be found in voids (1-5-4, 1-3-1 and 1-6-6; Fig. 1).

3.1.3. The melilite–spinel–hibonite inclusion

The melilite–spinel–hibonite inclusion 1-6-7 is a compact, irregularly shaped CAI fragment (Fig. 1d). The sub- to anhedral crystals of melilite (up to 20 μm in size) have compositions close to pure gehlenite and are set in aluminum–magnesium spinel. Voids are present and cracks run through the inclusion, but no alteration phases were observed. An irregular, foliated hibonite grain is found at the edge of the inclusion and a single RMN is located at a grain boundary between melilite and spinel (the composition of the RMN is reported in Schwander et al., 2015).

Table 1
Electron microprobe analyses for hibonite crystals in SHIBs and individual hibonite crystals.

Sample name	Grain[a]	Voltage (kV)	Ions per formula unit					Cation sum	Weight percentages of oxides					
			Ti[b]	Al	Mg	Ca	O		TiO_2	Al_2O_3	MgO	CaO	FeO[c]	Sum
SHIBs														
1-1-3	H1	20	0.78	10.48	0.66	1.00	19	13.0	9.2	79.3	3.9	8.4	b.d.	100.9
1-1-3	H2	20	0.81	10.40	0.68	1.01	19	12.9	9.6	78.7	4.1	8.4	0.04	100.9
1-1-7		20	0.48	11.00	0.51	0.97	19	13.0	5.7	82.8	3.0	8.0	0.08	99.6
1-1-8	H1	20	0.07	11.78	0.14	0.98	19	13.0	0.8	90.3	0.8	8.3	b.d.	100.3
1-1-8	H1	15	0.17	11.52	0.24	1.03	19	13.0	2.0	85.9	1.4	8.4	b.d.	97.8
1-1-8	H2	15	0.08	11.70	0.15	1.03	19	13.0	1.0	87.8	0.9	8.5	b.d.	98.2
1-1-9		15	0.12	11.66	0.18	1.01	19	13.0	1.4	88.2	1.1	8.4	0.15	99.3
1-1-12		20	0.75	10.44	0.72	1.08	19	13.0	8.7	77.9	4.2	8.9	0.05	99.8
1-2-7		15	0.79	10.42	0.73	1.01	19	13.0	9.1	77.1	4.3	8.2	b.d.	98.7
1-3-4	H1	15	0.11	11.74	0.13	1.01	19	13.0	1.3	88.8	0.8	8.4	b.d.	99.3
1-3-4	H1	15	0.12	11.72	0.13	1.03	19	13.0	1.4	87.8	0.8	8.5	b.d.	98.4
1-3-4	H1	15	0.12	11.73	0.13	1.02	19	13.0	1.4	88.4	0.8	8.4	b.d.	99.0
1-3-4	H2	15	0.10	11.75	0.11	1.05	19	13.0	1.1	88.7	0.7	8.7	b.d.	99.2
1-3-4	H3	15	0.14	11.67	0.16	1.03	19	13.0	1.7	87.7	1.0	8.5	b.d.	98.8
1-3-8		15	0.13	11.66	0.18	0.99	19	13.0	1.5	88.9	1.1	8.3	0.21	100.0
1-3-9	H1	15	0.31	11.27	0.35	1.03	19	13.0	3.6	84.3	2.1	8.5	b.d.	98.5
1-3-9	H2	15	0.34	11.21	0.37	1.03	19	13.0	4.0	83.4	2.2	8.5	b.d.	98.1
1-4-4		15	0.64	10.68	0.63	1.02	19	13.0	7.4	79.1	3.7	8.3	b.d.	98.5
1-5-2	H1	15	0.61	10.78	0.58	1.01	19	13.0	7.2	81.1	3.5	8.4	b.d.	100.2
1-5-2	H2	15	0.73	10.54	0.66	1.03	19	13.0	8.5	78.9	3.9	8.5	b.d.	99.8
1-5-2	H3	15	0.71	10.58	0.67	1.01	19	13.0	8.4	79.1	3.9	8.3	b.d.	99.8
1-5-2	H4	15	0.63	10.69	0.62	1.01	19	13.0	7.4	80.0	3.7	8.3	b.d.	99.3
1-5-4		15	0.53	10.89	0.53	1.02	19	13.0	6.2	81.9	3.1	8.4	b.d.	99.8
1-5-4		15	0.28	11.34	0.30	1.08	19	13.0	3.2	84.4	1.8	8.8	b.d.	98.2
1-5-4		15	0.28	11.35	0.30	1.06	19	13.0	3.3	84.3	1.8	8.6	b.d.	98.0
1-6-3		15	0.45	11.02	0.50	0.99	19	13.0	5.3	83.0	3.0	8.2	b.d.	99.5
1-6-4	H1	15	0.41	11.10	0.44	0.99	19	13.0	4.9	83.7	2.6	8.2	0.11	99.4
1-6-4	H1	15	0.33	11.28	0.35	1.02	19	13.0	3.9	85.1	2.1	8.4	b.d.	99.6
1-6-4	H2	15	0.31	11.35	0.32	1.01	19	13.0	3.6	85.8	1.9	8.4	b.d.	99.7
1-6-4	H2	15	0.14	11.68	0.16	1.02	19	13.0	1.7	89.0	0.9	8.6	b.d.	100.2
1-6-4	H3	15	0.19	11.57	0.21	1.02	19	13.0	2.3	87.6	1.2	8.5	b.d.	99.6
1-6-4	H3	15	0.26	11.44	0.26	1.02	19	13.0	3.1	86.4	1.6	8.5	b.d.	99.5
1-6-6	H1	15	0.25	11.42	0.28	1.01	19	13.0	3.0	86.7	1.7	8.4	b.d.	99.9
1-6-6	H1	15	0.02	11.88	0.07	1.01	19	13.0	0.2	90.2	0.4	8.4	b.d.	99.3
1-6-6	H2	15	0.17	11.54	0.23	1.02	19	13.0	2.0	86.8	1.3	8.4	b.d.	98.6
1-6-6	H2	15	0.19	11.54	0.23	1.01	19	13.0	2.3	87.3	1.4	8.4	b.d.	99.4
1-6-6	H3	15	0.26	11.26	0.34	1.01	19	13.0	3.0	84.1	2.0	8.3	0.39	97.8
1-6-6	H3	15	0.25	11.41	0.29	1.01	19	13.0	3.0	86.1	1.7	8.3	0.08	99.2
1-6-8		15	0.38	11.04	0.45	1.02	19	13.0	4.5	82.5	2.7	8.3	0.38	98.3
1-7-4		15	0.32	11.33	0.34	0.99	19	13.0	3.8	84.8	2.0	8.2	b.d.	98.7
1-9-5	H1	20	0.57	10.88	0.52	0.99	19	13.0	6.7	81.6	3.1	8.2	b.d.	99.6

Table 1 (continued)

Sample name	Grain[a]	Voltage (kV)	Ions per formula unit					Cation sum	Weight percentages of oxides					
			Ti[b]	Al	Mg	Ca	O		TiO_2	Al_2O_3	MgO	CaO	FeO[c]	Sum
1-9-5	H2	20	0.30	11.35	0.34	0.99	19	13.0	3.6	86.0	2.0	8.2	b.d.	99.8
1-10-5		20	0.47	11.07	0.43	0.99	19	13.0	5.7	84.3	2.6	8.3	b.d.	100.9
1-10-5		20	0.02	11.90	0.06	1.01	19	13.0	0.2	91.0	0.4	8.5	b.d.	100.0
1-10-5		20	0.20	11.58	0.20	1.02	19	13.0	2.4	88.7	1.2	8.6	b.d.	100.9
1-10-5		20	0.44	11.11	0.42	0.99	19	13.0	5.3	84.6	2.5	8.2	b.d.	100.6
1-10-5		20	0.50	11.03	0.44	0.98	19	13.0	5.9	83.9	2.7	8.2	b.d.	100.7
1-10-5		20	0.20	11.54	0.23	0.99	19	13.0	2.4	88.4	1.4	8.4	b.d.	100.5
1-10-6		20	0.90	10.28	0.75	0.97	19	12.9	10.7	78.0	4.5	8.1	b.d.	101.3
Single hibonite crystals														
1-9-2		20	0.41	11.14	0.40	1.01	19	13.0	4.8	84.0	2.4	8.4	b.d.	99.6
2-2-3		20	0.77	10.49	0.68	0.99	19	12.9	9.0	79.1	4.1	8.2	b.d.	100.4
1-6-2		15	0.51	10.98	0.46	1.02	19	13.0	5.9	81.8	2.7	8.3	b.d.	98.7

[a] H + number indicates analyzed hibonite grain; same number means same grain.
[b] Sum of Ti^{4+} and Ti^{3+}.
[c] b.d. = below detection limit.

3.2. Oxygen isotopes

The oxygen isotopic compositions of the 33 analyzed SHIBs are summarized in Table 3. The SHIBs yield an average $\Delta^{17}O$ value of $-23.4 \pm 1.1‰$ (± 2 SD). Plotted in a oxygen three-isotope diagram, the SHIBs form a tight cluster (Fig. 3) close to the CCAM (carbonaceous chondrite anhydrous mineral; Clayton et al., 1977) line. While many SHIB analyses overlap with the CCAM line within uncertainty, they are, on average, displaced toward heavier compositions by $\sim 1‰$ amu^{-1}. In contrast, the SHIB cluster falls on the primitive chondrule mixing (PCM, Ushikubo et al., 2012) line (Fig. 3b). The three MgO-rich single hibonite crystals and the melilite–spinel–hibonite inclusion (1-6-7) plot within the SHIB cluster (Fig. 3b).

Results of oxygen isotope standard analyses are presented in Electronic appendix EA.2.

3.3. Magnesium isotopes

Both hibonite and spinel grains in SHIBs show variations in $\delta^{25}Mg$ values, which may be evidence for mass-dependent isotope fractionation (Table 4). The magnitudes of $\delta^{25}Mg$ values are within $\pm 5‰$ for seven of the eight studied SHIBs, only 1-10-5 has larger enrichments in ^{25}Mg ($\delta^{25}Mg$ of ~ 8–$13‰$ for hibonite, $\sim 18‰$ for spinel). Within the same CAI, there is no variation beyond 2σ for spinel analyses (Table 4), while variations in $\delta^{25}Mg$ are resolvable in hibonite in two SHIBs (1-6-6 and 1-10-5). Spinel analyses are usually slightly more enriched in ^{25}Mg than hibonite analyses within the same SHIB (exception is SHIB 1-2-1), which could be a bias introduced by the two standards (see Section 4). Results of magnesium isotope standard analyses are presented in Electronic appendix EA.3.

Fig. 4 shows that for seven of the eight studied SHIBs, spinel and hibonite analyses fall on a well-defined multi-CAI mineral isochron (MSWD 1.07) with a slope corresponding to an initial $^{26}Al/^{27}Al$ ratio of $(4.8 \pm 0.1) \times 10^{-5}$ and an initial $\delta^{26}Mg_0^*$ marginally resolved from zero (i.e., $0.07 \pm 0.05‰$). Internal isochrons of these seven SHIBs, constructed from two to five analyses within the same SHIB, give initial $^{26}Al/^{27}Al$ ratios between $(4.6 \pm 0.6) \times 10^{-5}$ to $(5.3 \pm 1.1) \times 10^{-5}$, some within 2σ uncertainty of and others below the canonical ratio (Table 4, Fig. 5). In contrast, the slope of the isochron for SHIB 1-3-9, in which only one hibonite and one spinel analysis could be collected, yields a significantly smaller initial $^{26}Al/^{27}Al$ ratio of $(2.5 \pm 0.7) \times 10^{-5}$ and a higher initial $\delta^{26}Mg^*$ of $0.8 \pm 0.2‰$ (Fig. 4b).

Hibonite analyses show a wide range of $^{27}Al/^{24}Mg$ ratios from ~ 25 to ~ 133 (Table 4). In contrast, spinel analyses show less variation, most have a ratio of ~ 2.6, only spinel analyses in 1-10-5 and in 1-2-1 have a ratio of ~ 2.8.

3.4. Calcium and titanium isotopes

None of the five SHIBs studied for calcium and titanium isotopes show mass-independent anomalies in calcium or titanium isotopes beyond the 3σ level, independent of the isotope pair chosen for normalization (Table 5). However,
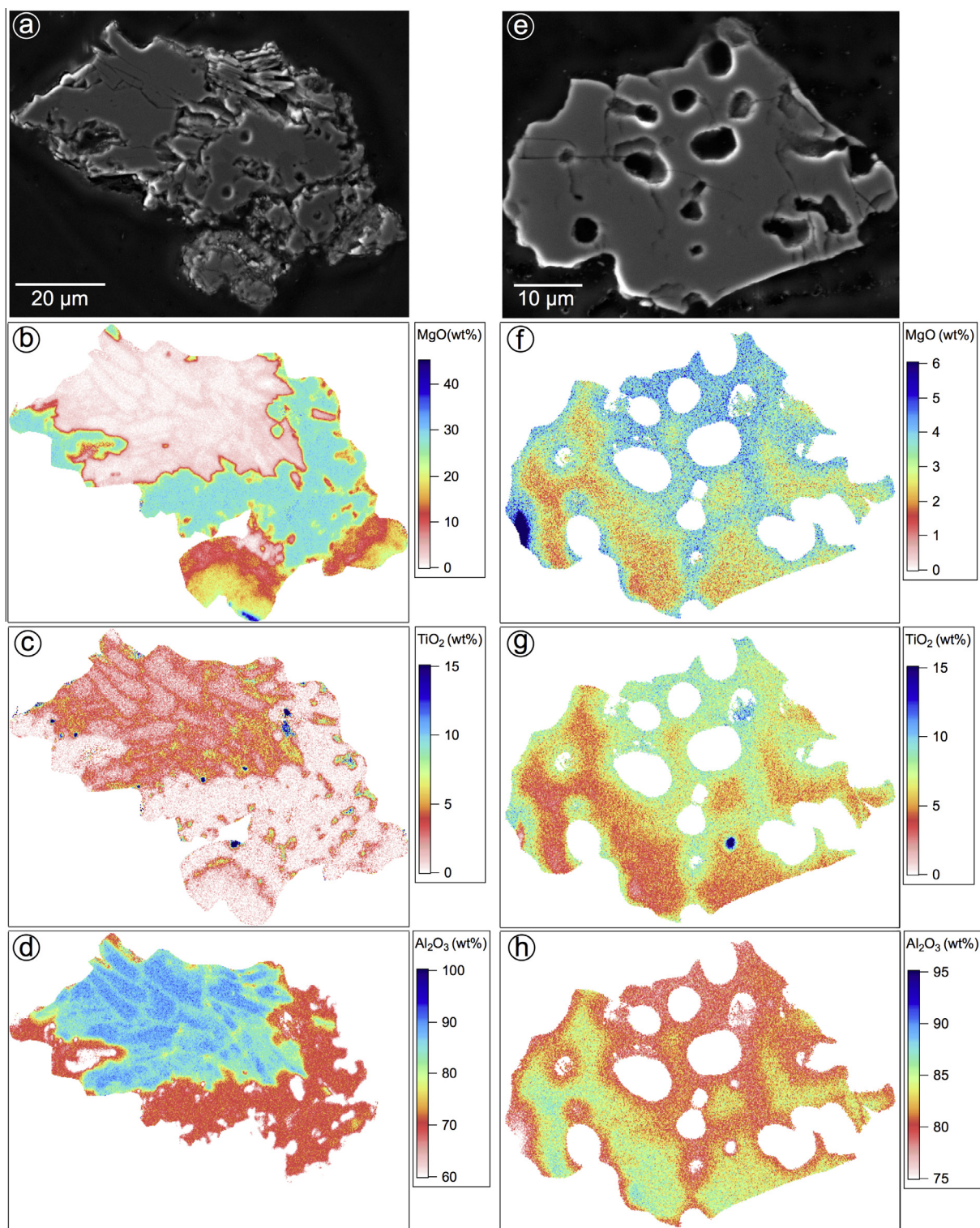
Fig. 2. SE images and MgO, TiO₂, and Al₂O₃ quantitative elemental maps for SHIB 1-6-4 (a–d) and MgO-rich hibonite crystal 2-2-8 (e–h). The maps for 1-6-4 (b–d) show that individual hibonites are zoned in Al₂O₃, MgO and TiO₂. Hibonite grain centers are generally more Al₂O₃-rich and MgO- and TiO₂-poor than rims. While hibonite grain 2-2-8 is also zoned, the zoning does not appear to be concentric (f–h). The top of the grain and regions around voids are more enriched in MgO and TiO₂ than the lower part of the grain.

Table 2
Averages of energy dispersive spectroscopy analyses of spinel grains, presented as cation numbers per four oxygens. A detailed data table can be found in Electronic appendix EA.1.

Name	N^a	Number of cations per 4 oxygen								Al + Cr+ V + Ti + Si	2SD[b]	Mg+ Fe + Ca	2SD
		Ti^{4+}	V^{3+}	Al^{3+}	Mg^{2+}	Si^{4+}	Ca^{2+}	Cr^{3+}	Fe^{2+}				
EPMA standard	12	0.00	0.00	1.99	1.00	0.00	0.00	0.00	0.00	2.00		0.00	1.00	0.01
Burma spinel	9	0.00	0.00	1.98	1.00	0.00	0.00	0.01	0.00	2.00		0.01	1.00	0.01
Spinel in CAIs[c]	46	0.00	0.00	1.98	1.00	0.00	0.00	0.00	0.00	2.00		0.01	1.00	0.01
Spinel in 1-10-5	7	0.00	0.02	2.02	0.93	0.00	0.00	0.00	0.00	2.04		0.01	0.93	0.02

[a] N indicates number of analyses collected.
[b] Two standard deviations.
[c] Average of analyses collected in SHIBs 1-2-1, 1-3-1, 1-3-9, 1-5-4, 1-6-6, and melilite-bearing spinel-hibonite inclusion 1-6-7.

Table 3
Oxygen isotope data for SHIBs, single hibonite crystals and the melilite-spinel-hibonite CAI separated from the Murchison meteorite. Data are averages from spinel, hibonite and/or melilite analyses. Uncertainties are 2σ.

Sample name	N^a	$\delta^{18}O$ (‰)	$\delta^{17}O$ (‰)	$\Delta^{17}O$ (‰)
SHIBs				
1-1-3	2	−44.7 ± 0.9	−46.1 ± 2.0	−22.9 ± 1.6
1-1-6	3	−44.5 ± 0.8	−46.2 ± 1.4	−23.1 ± 1.1
1-1-7	4	−44.2 ± 0.7	−45.7 ± 0.8	−22.7 ± 1.0
1-1-8	4	−45.7 ± 1.0	−46.7 ± 0.7	−23.0 ± 0.6
1-1-9	2	−43.9 ± 1.3	−46.4 ± 1.5	−23.5 ± 0.9
1-1-12	3	−44.0 ± 1.1	−46.7 ± 0.7	−23.8 ± 0.6
1-1-14	1	−43.8 ± 1.1	−47.0 ± 1.0	−24.2 ± 0.9
1-2-1	3	−44.2 ± 1.1	−47.2 ± 0.6	−24.3 ± 0.9
1-2-2	2	−45.5 ± 0.9	−47.5 ± 0.7	−23.9 ± 1.0
1-2-7	5	−45.0 ± 1.2	−47.2 ± 0.7	−23.8 ± 0.5
1-3-1	2	−45.3 ± 1.2	−46.4 ± 1.3	−22.8 ± 0.9
1-3-4	2	−42.6 ± 1.2	−44.1 ± 0.7	−22.0 ± 0.8
1-3-6	2	−43.0 ± 1.2	−44.8 ± 1.0	−22.5 ± 1.3
1-3-7	4	−44.3 ± 0.9	−46.9 ± 0.5	−23.8 ± 0.6
1-3-8	2	−45.1 ± 1.1	−46.9 ± 0.8	−23.5 ± 0.8
1-3-9	4	−43.9 ± 1.9	−46.5 ± 1.8	−23.7 ± 1.0
1-3-10	2	−44.6 ± 1.1	−45.9 ± 0.7	−22.7 ± 0.8
1-3-11	1	−44.4 ± 1.3	−47.6 ± 0.8	−24.5 ± 1.0
1-4-4	3	−44.1 ± 0.7	−46.5 ± 1.0	−23.6 ± 1.0
1-4-6	3	−44.6 ± 0.6	−47.3 ± 0.7	−24.1 ± 0.8
1-5-1	3	−44.7 ± 1.4	−46.5 ± 1.2	−23.3 ± 0.7
1-5-2	2	−45.3 ± 1.1	−47.2 ± 0.8	−23.6 ± 0.8
1-5-4	4	−44.6 ± 1.1	−46.8 ± 0.9	−23.6 ± 0.7
1-6-3	3	−43.2 ± 1.1	−45.8 ± 1.1	−23.3 ± 0.8
1-6-4	2	−44.8 ± 0.8	−46.5 ± 0.7	−23.2 ± 0.8
1-6-5	2	−44.2 ± 0.7	−46.7 ± 0.8	−23.7 ± 0.9
1-6-6	4	−44.7 ± 1.0	−46.3 ± 0.6	−23.0 ± 0.9
1-6-8	2	−44.8 ± 0.9	−46.7 ± 0.8	−23.4 ± 0.7
1-7-4	2	−44.7 ± 0.9	−46.9 ± 0.6	−23.7 ± 1.0
1-9-5	3	−43.7 ± 0.6	−45.3 ± 0.8	−22.6 ± 0.7
1-10-4	3	−44.3 ± 1.0	−46.0 ± 1.3	−23.0 ± 1.1
1-10-5	4	−43.1 ± 0.6	−46.2 ± 1.1	−23.8 ± 0.9
1-10-6	2	−44.3 ± 0.7	−46.4 ± 0.6	−23.4 ± 0.4
Single hibonite crystals				
1-9-2	2	−44.0 ± 0.8	−46.5 ± 1.0	−23.6 ± 0.8
2-2-3	1	−44.2 ± 0.7	−46.5 ± 1.3	−23.5 ± 1.4
1-6-2	2	−43.0 ± 0.8	−46.2 ± 0.7	−23.9 ± 0.8
Melilite-spinel-hibonite inclusion				
1-6-7	4	−44.4 ± 0.7	−46.9 ± 0.7	−23.8 ± 0.6

[a] N indicates number of individual analyses used to calculate average.

the average $\delta^{50}Ti$ value calculated from the five SHIB analyses is positive, 2.4 ± 1.0‰ (2SE; $^{46}Ti/^{48}Ti$ normalization). The average $\delta^{48}Ca$ value is unresolved from terrestrial (−0.1 ± 1.1‰).

The five studied SHIBs show no evidence for high degrees of mass-dependent fractionation in calcium or titanium. SHIB 1-5-4 appears to be isotopically heavy in both titanium and calcium by 1–2‰ amu^{-1} (Table 5). SHIB 1-3-7 has a positive F_{Ti} value that is marginally resolved beyond the 3σ level ($^{46}Ti/^{48}Ti$ normalization), all other SHIBs lack clearly resolved effects in calcium and titanium beyond the 3σ level (Table 5).

Results of calcium and titanium isotope standard analyses are presented in Electronic appendix EA.4.

4. DISCUSSION

4.1. Formation, alteration, classification

4.1.1. Relationship between petrologic features and stable isotopes

For some SHIBs, a melt origin is indicated by petrologic or stable isotopic characteristics. For example, SHIBs 1-6-6, 1-1-8 and 1-5-4 have rounded outer shapes, consistent with crystallization from a melt droplet. Other SHIBs (e.g., 1-2-1 and 1-10-5) show heavy magnesium isotope enrichments (positive $\delta^{25}Mg$) in both spinel and hibonite grains, consistent with partial magnesium evaporation during melting. However, there is no general correlation between these properties. For example, rounded SHIB 1-6-6 is isotopically light compared to other SHIBs (Table 4), suggesting that its magnesium isotopic signature is dominated by condensation rather than melt evaporation (e.g., Richter et al., 2002). The formation mechanisms of these SHIBs and consistency between stable isotopic signatures are further discussed in Section 4.3.

4.1.2. Alteration

Voids are a common feature in many SHIBs. While sample preparation like acid-treatment or polishing can remove soluble phases or individual minerals from these inclusions, many voids are filled with alteration phases or epoxy, suggesting they were not introduced by polishing. A comparison of acid-treated and untreated SHIBs shows that the acid effectively removed primary and secondary silicate phases. In addition, hibonite–hibonite and spinel–spinel
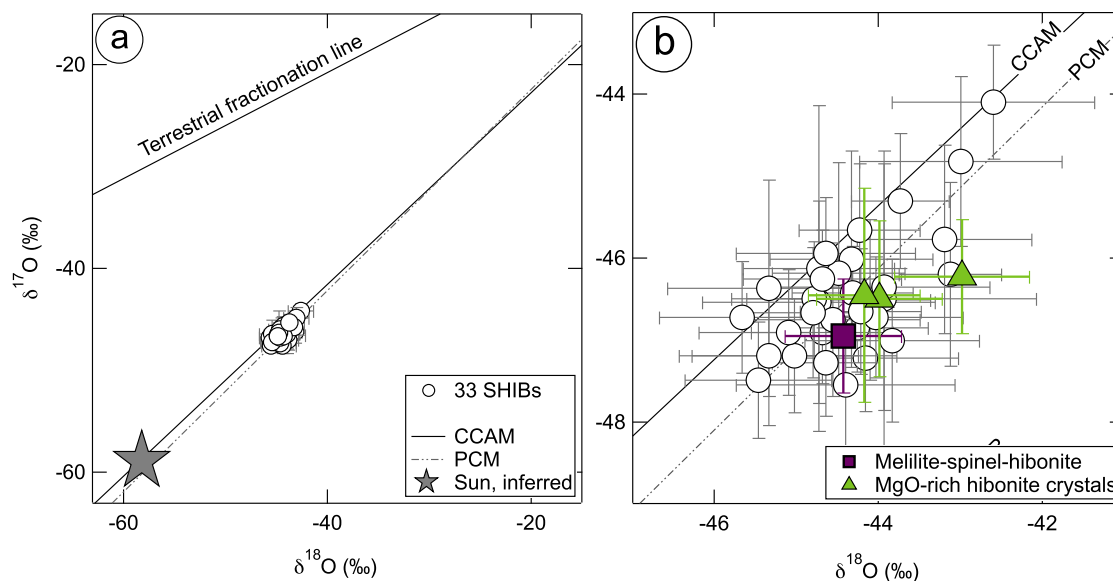
Fig. 3. Average oxygen isotope compositions of SHIBs. (a) The 33 analyzed SHIBs are ^{16}O-rich relative to the terrestrial fractionation line, but ^{16}O-depleted relative to the inferred value for the Sun (McKeegan et al., 2011). Notably, the SHIBs define a tight cluster near the CCAM (carbonaceous chondrite anhydrous mineral) and PCM (primitive chondrule mixing) lines. (b) Enlargement of the SHIB region. The melilite-spinel-hibonite inclusion (1-6-7) and three MgO-rich single hibonite crystals plot in the SHIB cluster. The latter could be fragments of SHIBs. Plotted uncertainties are 2σ.

grain boundaries are more easily recognizable in acid-treated SHIBs (e.g., 1-1-8 in Fig. 1), which could be a result of dissolution of interstitial silicate minerals or etching of oxide minerals. However, the presence of alteration phases inside untreated SHIBs (e.g., 1-5-4 and 1-3-1 in Fig. 1) suggests that some porosity is primary or was caused by fluid-assisted alteration on the parent body. Spinel in the CAIs is close to end-member composition and abundances of FeO are usually below detection limit in hibonite, supporting the pristine character of the primary minerals that we have studied for their isotope characteristics.

4.1.3. A note on classification

We studied 78 hibonite-rich CAIs for their isotopic and petrologic characteristics (37 are presented here, others have been described in Kööp et al., 2014a,b, 2015). Most of these CAIs fall into two isotopic groups, i.e., SHIBs and PLACs, as defined by Ireland (1988). Similar to Ireland (1988), we find that the presence of both spinel and hibonite is a good first indicator, but not sufficient, for grouping a hibonite-rich CAI with the SHIBs. Classification based on the presence of spinel fails, for example, in the case of four spinel-bearing hibonite-rich CAIs that share isotopic and chemical characteristics with PLAC-like CAIs (Kööp et al., 2014a) and for spinel-free hibonite crystals that were separated from SHIBs, possibly by laboratory disaggregation of the host meteorite. In the absence of isotopic data, the best proxy for estimating the isotopic character and classifying the CAI is hibonite mineral chemistry. In particular, it is the zonation in hibonite minerals (Fig. 2) which distinguishes SHIB hibonites from the uniformly MgO-poor PLAC hibonites, in addition to the larger range of MgO contents noted by Ireland (1988) and also indicated in Table 1. Similarly, lower MgO contents

than those typical for PLAC and SHIB hibonites are good indicators for a melt evaporation origin of a hibonite grain. Based on these considerations, three irregularly shaped, spinel-free hibonite crystals were included in this study (Figs. 1b, 2e–h), which share isotopic, chemical and morphological characteristics with SHIB hibonites (Fig. 3b) and could have been liberated from SHIBs during freeze–thaw disaggregation or acid treatment.

4.2. Individual isotopic systems

4.2.1. Oxygen isotopes

The tight clustering of the SHIBs at a Δ^{17}O of −23.4 ± 1.1‰ suggests that these objects formed in a reservoir that had a uniform distribution of oxygen isotopes, but was slightly depleted in ^{16}O compared to the inferred solar value (−28.4 ± 1.8‰, 2σ; McKeegan et al., 2011). The average Δ^{17}O of approximately −23‰ is in excellent agreement with that of many other CAIs from CR chondrites, the ungrouped primitive chondrite Acfer 094 and certain primary minerals like hibonite or spinel in CV chondrite CAIs (Makide et al., 2009; Ushikubo et al., 2011; Bullock et al., 2012). However, small differences between the datasets exist, i.e., Acfer 094 CAIs are slightly more spread out along the CCAM line than SHIBs (i.e., larger variation in Δ^{17}O; Ushikubo et al., 2011) and CR CAIs show a larger range of mass-dependent fractionation when compared to SHIBs, possibly due to melt evaporation (Makide et al., 2009), which could indicate that CR CAIs experienced higher degrees of evaporation than SHIBs.

The uniformity in oxygen isotopes among the 33 SHIBs studied here is in clear contrast to SHIB data from Liu et al. (2009a), i.e., 12 SHIBs define a resolved Δ^{17}O range between about −27‰ and −15‰. As illustrated in

Table 4
Magnesium isotope analyses for the eight SHIBs which allowed separate analyses of spinel and hibonite grains. Uncertainties are 2σ.

Name	Phase[a]	Spot[b]	Session[c]	Cycles[d]	Standard[e]	$\delta^{25}Mg$ (‰)	$\delta^{26}Mg$ (‰)	$^{27}Al/^{24}Mg$	$\delta^{26}Mg^*$ (‰)	$^{26}Al/^{27}Al$ (10^{-5}) Model[f]	$^{26}Al/^{27}Al$ (10^{-5}) Internal[g]	$\delta^{26}Mg_0^*$ (‰)	MSWD
1-1-8	sp	G 1	July14	30	sp	1.3 ± 0.1	3.5 ± 0.3	2.6 ± 0.0	0.9 ± 0.1		4.7 ± 0.2	0.07 ± 0.11	1.3
	sp	G 2	July14	30	sp	1.5 ± 0.1	3.9 ± 0.3	2.6 ± 0.0	1.0 ± 0.1				
	hib	G 1	Feb14	199	hib	0.0 ± 1.2	33.1 ± 1.2	94.1 ± 2.7	33.3 ± 2.4	4.9 ± 0.4			
	hib	G 2	Feb14	199	hib	−1.5 ± 0.7	34.3 ± 0.7	112.1 ± 1.2	37.4 ± 1.3	4.6 ± 0.2			
1-10-5	sp	S 1	July14	30	sp	17.8 ± 0.2	36.0 ± 0.2	2.8 ± 0.0	1.1 ± 0.2		4.9 ± 0.2	0.12 ± 0.12	0.4
	sp	S 2	July14	30	sp	17.8 ± 0.2	36.2 ± 0.2	2.8 ± 0.0	1.1 ± 0.2				
	hib	G 1	Feb14	199	hib	13.1 ± 1.0	72.0 ± 1.0	133.1 ± 2.0	46.3 ± 2.1	4.8 ± 0.2			
	hib	G 2	Feb14	100	hib	7.7 ± 0.8	27.0 ± 0.8	32.2 ± 0.3	12.0 ± 2.0	5.2 ± 0.8			
	hib	G 3	Feb14	199	hib	9.6 ± 0.5	40.1 ± 0.5	59.7 ± 0.6	21.2 ± 1.1	5.0 ± 0.3			
1-2-1	sp		July14	30	sp	0.6 ± 0.2	2.0 ± 0.2	2.8 ± 0.0	0.9 ± 0.2		4.6 ± 0.5	−0.03 ± 0.20	0.3
	hib	S 1	Feb14	199	hib	3.6 ± 0.8	20.3 ± 0.8	39.3 ± 0.5	13.3 ± 1.5	4.7 ± 0.5			
	hib	S 2	Feb14	99	hib	3.3 ± 0.6	14.7 ± 0.6	25.4 ± 0.3	8.1 ± 1.3	4.5 ± 0.7			
1-3-1	sp		July14	30	sp	−1.3 ± 0.2	−1.6 ± 0.2	2.6 ± 0.0	0.9 ± 0.2		5.3 ± 1.1	−0.10 ± 0.26	
	hib		Feb14	199	hib	−4.0 ± 1.1	3.6 ± 1.1	30.7 ± 0.4	11.5 ± 1.8	5.2 ± 0.8			
1-3-9	sp		July14	30	sp	−0.2 ± 0.2	0.8 ± 0.2	2.6 ± 0.0	1.3 ± 0.2		2.5 ± 0.7	0.79 ± 0.21	
	hib		Feb14	99	hib	−1.4 ± 0.8	3.9 ± 0.8	32.6 ± 0.3	6.6 ± 1.5	2.8 ± 0.7			
1-5-4	sp		July14	30	sp	3.1 ± 0.2	7.0 ± 0.2	2.6 ± 0.0	0.9 ± 0.2		4.9 ± 0.4	0.04 ± 0.18	0.2
	hib	S 1	Feb14	199	hib	0.4 ± 0.8	17.1 ± 0.8	45.7 ± 0.5	16.2 ± 1.5	4.9 ± 0.5			
	hib	S 2	Feb14	99	hib	0.9 ± 1.0	16.5 ± 1.0	43.4 ± 0.5	14.8 ± 2.0	4.8 ± 0.6			
1-6-6	sp		July14	30	sp	−1.5 ± 0.1	−1.9 ± 0.3	2.6 ± 0.0	1.1 ± 0.1		4.7 ± 0.3	0.19 ± 0.16	3.5
	hib	G 1	Feb14	199	hib	−2.0 ± 0.7	8.3 ± 0.7	38.5 ± 0.4	12.1 ± 1.3	4.4 ± 0.5			
	hib	G 2	Feb14	199	hib	−3.9 ± 0.8	15.1 ± 0.8	64.8 ± 0.7	22.8 ± 1.5	4.9 ± 0.3			
1-7-4	sp	S 1	July14	30	sp	−1.5 ± 0.2	−2.1 ± 0.2	2.6 ± 0.0	0.9 ± 0.2		4.6 ± 0.6	0.10 ± 0.16	0.9
	sp	S 2	July14	30	sp	−1.7 ± 0.2	−2.3 ± 0.2	2.6 ± 0.0	1.0 ± 0.2				
	hib		Feb14	199	hib	−2.4 ± 0.9	9.2 ± 0.9	42.4 ± 0.5	14.0 ± 1.6	4.6 ± 0.5			

[a] Phase analyzed, sp = spinel, hib = hibonite.
[b] G indicates analyses in different grains, S indicates analyses in same grain, but different spot.
[c] SIMS analysis session.
[d] Number of cycles included in average.
[e] Standard used.
[f] Inferred from model isochron.
[g] Inferred from internal isochron.

Table 5

Titanium and calcium isotope analyses for five SHIBs. Titanium data is listed in the two commonly used normalizations. F_{Ti} and F_{Ca} indicate intrinsic fractionation in ‰ per atomic mass unit (amu). Uncertainties are 2σ.

Sample name	F_{Ti} (‰/amu)	$\delta^{47}Ti$ (‰)	$\delta^{49}Ti$ (‰)	$\delta^{50}Ti$ (‰)
$^{46}Ti/^{48}Ti$ normalization				
1-10-5	0.4 ± 0.7	-1.1 ± 1.7	-2.4 ± 2.4	0.7 ± 2.4
1-3-4	0.9 ± 0.9	1.3 ± 2.2	-1.2 ± 2.9	3.2 ± 3.2
1-3-7	1.4 ± 0.8	0.9 ± 2.0	0.1 ± 2.3	3.6 ± 2.4
1-3-9	0.1 ± 0.7	0.2 ± 1.9	0.1 ± 2.1	1.8 ± 2.2
1-5-4	1.8 ± 0.7	-0.3 ± 1.8	-1.2 ± 2.2	2.8 ± 2.2

Sample name	F_{Ti} (‰/amu)	$\delta^{46}Ti$ (‰)	$\delta^{48}Ti$ (‰)	$\delta^{50}Ti$ (‰)
$^{49}Ti/^{47}Ti$ normalization				
1-10-5	-0.4 ± 0.9	0.4 ± 1.9	1.7 ± 1.8	4.3 ± 3.1
1-3-4	-0.2 ± 1.4	-1.9 ± 2.8	-0.2 ± 2.4	5.5 ± 5.0
1-3-7	1.0 ± 1.0	-1.1 ± 2.5	-0.5 ± 2.1	3.9 ± 3.5
1-3-9	0.1 ± 0.8	-0.1 ± 2.1	-0.2 ± 1.9	1.7 ± 2.8
1-5-4	1.4 ± 1.0	0.0 ± 2.1	0.7 ± 1.9	4.6 ± 3.4

Sample name	F_{Ca} (‰/amu)	$\delta^{42}Ca$ (‰)	$\delta^{43}Ca$ (‰)	$\delta^{48}Ca$ (‰)
Calcium data				
1-10-5	-1.1 ± 0.9	0.6 ± 2.4	2.2 ± 3.1	0.7 ± 4.7
1-3-4	0.4 ± 0.9	-0.4 ± 2.7	-0.4 ± 3.2	1.5 ± 4.6
1-3-7	1.3 ± 0.9	0.3 ± 2.6	0.8 ± 3.2	-0.6 ± 4.5
1-3-9	0.1 ± 0.9	0.1 ± 2.5	-0.2 ± 2.8	0.0 ± 4.4
1-5-4	2.1 ± 1.0	-1.1 ± 2.7	-1.7 ± 3.2	-1.9 ± 4.6
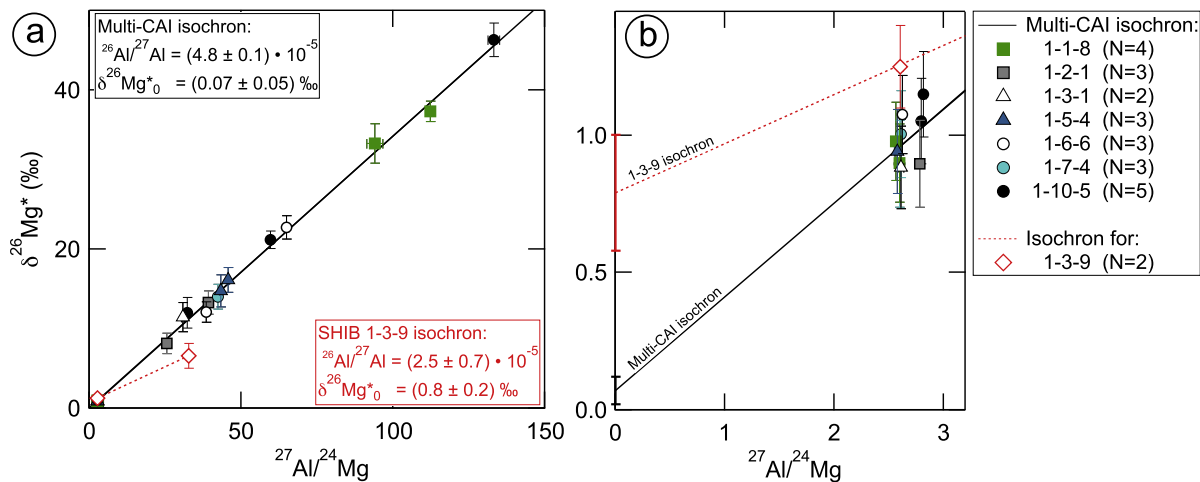
Fig. 4. Aluminum–magnesium data for eight SHIBs. (a) Individual mineral analyses of seven SHIBs fall on a single, multi-CAI mineral isochron with an MSWD of 1.07. Only the hibonite analysis of SHIB 1-3-9 is clearly below this line. (b) An enlargement of the spinel region from (a) shows that the intercept of the 1-3-9 isochron is at a higher $\delta^{26}Mg_0^*$ (0.8 ± 0.2‰), consistent with remelting of a refractory precursor after significant decay of ^{26}Al. Plotted uncertainties are 2σ.

Fig. 6a, the lowest $\Delta^{17}O$ value of the Liu et al. (2009a) dataset is defined by an object that is offset from the CCAM line. Aside from this grain, most CAIs that are distinct from the cluster defined by our SHIBs are comparably depleted in ^{16}O. The reason for the discrepancy between the two datasets is unclear. However, we are confident that the data presented in this study is accurate (frequent analysis of bracketing standards, use of appropriate mineral standards,

high spatial resolution that prevented sampling of alteration phases, which was confirmed by post-SIMS SEM work). It is unlikely that we sampled uniform SHIBs by chance, as the number of SHIBs studied here is higher than the number of SHIBs studied by Liu et al. (2009a).

Our new results show for the first time that SHIBs and PLAC-like CAIs have different oxygen isotopic characteristics (Fig. 6b). PLAC-like CAIs that were analyzed in the
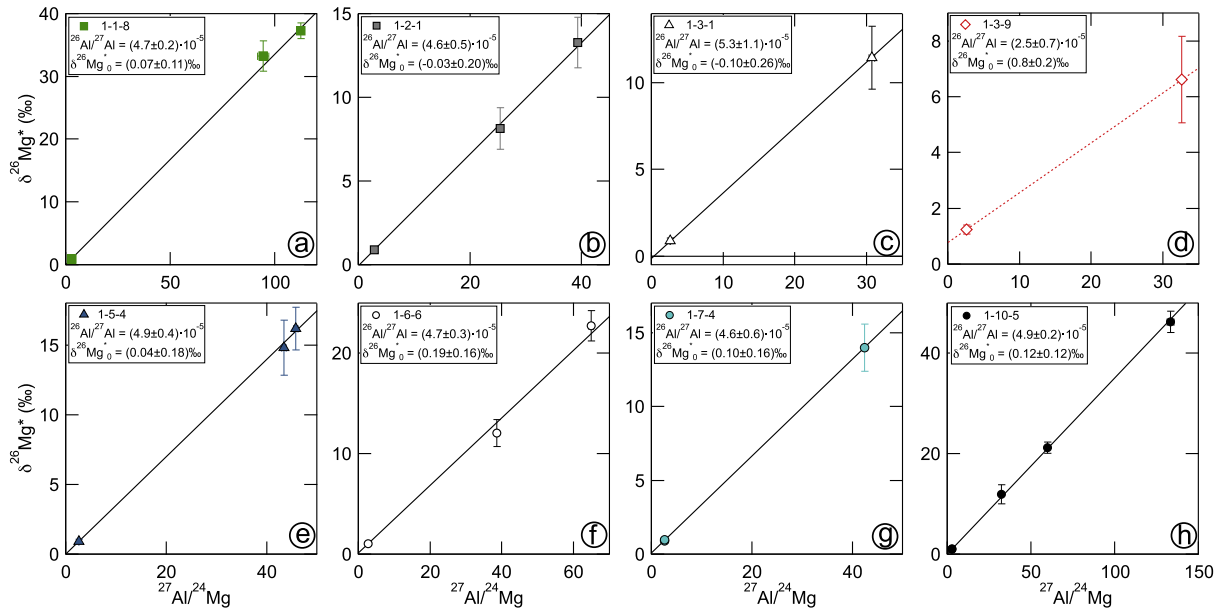
Fig. 5. Internal isochrons constructed from individual spinel and hibonite analyses for eight SHIBs. Plotted uncertainties are 2σ.
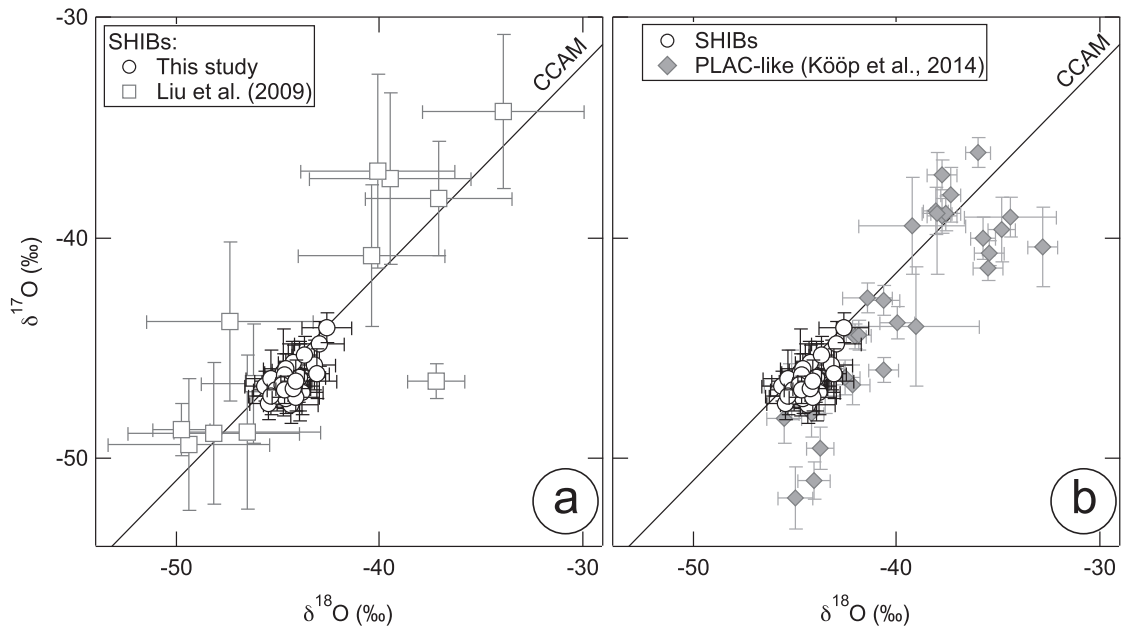

Fig. 6. Comparison of SHIB data obtained in this study with (a) SHIBs analyzed by Liu et al. (2009a) and with (b) PLAC-like CAIs. (a) The tight cluster defined by our analyses of 33 SHIBs is in clear contrast to the spread defined by 12 SHIB analyses from Liu et al. (2009a). (b) The clustering found in SHIBs is also in contrast to the spread defined by PLAC-like CAIs that were analyzed in the same session and under identical conditions as our SHIBs. Also, while many PLAC-like CAIs are resolved from the CCAM line, SHIBs are generally within uncertainty of this line. Plotted uncertainties are 2σ.

same session have larger variations in oxygen isotopes than SHIBs (^{17}O between ~-28 and $-17‰$, larger offsets from CCAM line; Kööp et al., 2014a), which was also found in PLACs studied by Liu et al. (2009a). Δ^{17}O fluctuations have been observed in some CAIs from CV and CO chondrites and have been attributed to coexisting ^{16}O-rich and ^{16}O-poor reservoirs (Itoh and Yurimoto, 2003; Simon et al.,

2011; Park et al., 2012). If true, the uniform Δ^{17}O values found in many CAIs from primitive chondrites (e.g., SHIBs, CR CAIs and Acfer 094 CAIs, as well as certain primary minerals in primitive CV chondrites) are remarkable. CAIs with Δ17O values of approximately $-23‰$ are not only abundant in primitive meteorites, but they also show a wide range of petrologic characteristics. For example,

SHIBs, CR and Acfer 094 CAIs are small compared to CV CAIs, and while melilite is a common mineral in many of these CAIs, it is absent in most SHIBs. This diversity implies that oxygen isotopic reservoirs with a stable $\Delta^{17}O$ existed under a variety of physicochemical conditions. It further remains mysterious as to why $\Delta^{17}O$ values of SHIBs and other CAIs are commonly higher than the estimated solar value ($\Delta^{17}O$: –28.4 ± 1.8‰ McKeegan et al., 2011).

4.2.2. Aluminum and magnesium isotopes and ^{26}Al–^{26}Mg systematics

The SHIBs show $\delta^{25}Mg$ variations in both hibonite and spinel, likely as a result of mass-dependent fractionation processes during their formation. While relative differences in $\delta^{25}Mg$ listed in Table 4 can be compared as a function of mineral type, the absolute values may suffer from a small bias that may have been introduced from using terrestrial hibonite and spinel mineral standards of unknown magnesium isotopic compositions for bracketing. To facilitate a comparison between hibonite and spinel analyses, the uncertainty in standard composition (conservative estimate of 1‰, see Section 2.5.2 and Luu et al., 2013) needs to be considered in addition to counting statistics. Doing so indicates that both hibonite and spinel grains in SHIBs 1-3-1, 1-6-6 and 1-7-4 are isotopically light in magnesium by ~1–4‰/amu (Fig. 7), potentially indicating a condensation signature (Richter et al., 2002). $\delta^{25}Mg$ values range from ~0 (1-3-9 and 1-1-8) to slightly positive values in 1-5-4 and 1-2-1 (Fig. 7). The highest $\delta^{25}Mg$ values are found in SHIB 1-10-5 (~8–18‰), consistent with significant loss of magnesium during melt evaporation (e.g., Mendybaev et al., 2013). The higher degree of mass-dependent fractionation in magnesium isotopes in 1-10-5 appears consistent with the nonstoichiometry in the spinel grain of this CAI, as both observations may be attributable to formation at higher temperatures than the other studied SHIBs (e.g., Simon et al., 1994). As indicated in Section 3.3, spinel

analyses appear to be isotopically heavier than hibonite analyses for all studied SHIBs except 1-2-1. However, except for 1-10-5, this difference is only marginal or is not resolved beyond the more conservative uncertainty estimate and could be a result of small differences in the isotopic compositions of the hibonite and the spinel standards.

The spread in $^{27}Al/^{24}Mg$ ratios in hibonites (Table 4) is consistent with variations seen in EPMA and EDS data, which suggest high degrees of coupled variability in MgO and Al_2O_3 contents within and among hibonite grains (e.g., Table 1). The analyzed spinel grains fall into two groups with regard to their $^{27}Al/^{24}Mg$ ratios. Most SHIB spinel grains have a ratio of ~2.6, but in 1-10-5 and 1-2-1, the ratio is ~2.8. For 1-2-1, the higher ratio is likely due to sampling of a small amount of adjacent hibonite, for 1–10-5 it is likely due to nonstoichiometry in the analyzed spinel.

Seven of the eight SHIBs show high $^{26}Al/^{27}Al$ ratios, which are, on average, slightly below the canonical $^{26}Al/^{27}Al$ ratio. In the Appendix, we assess the possibility that this small depletion could be the result of a bias in $^{27}Al/^{24}Mg$ ratios introduced by the matrix effect and find that a canonical incorporation of ^{26}Al cannot be excluded for these seven SHIBs. However, similarly high subcanonical levels of ^{26}Al are typical in Acfer 094 CAIs (Ushikubo et al., 2011) and are also observed in some CR chondrite CAIs (Makide et al., 2009). As these CAIs typically have similar $\Delta^{17}O$ values as the SHIBs studied here, it may further emphasize the isotopic similarity among these materials and possibly support the high, yet slightly subcanonical ratio in these seven SHIBs. In contrast, the low ratio inferred for SHIB 1-3-9 is clearly subcanonical (i.e., (2.5 ± 0.7) × 10^{-5}; Figs. 4, 5d) and no evidence for alteration was found in this CAI. Subcanonical ratios may be a result of early formation during admixture of ^{26}Al, as suggested by Liu et al. (2012), or may be due to late formation or resetting after partial decay of ^{26}Al. The shallow slope
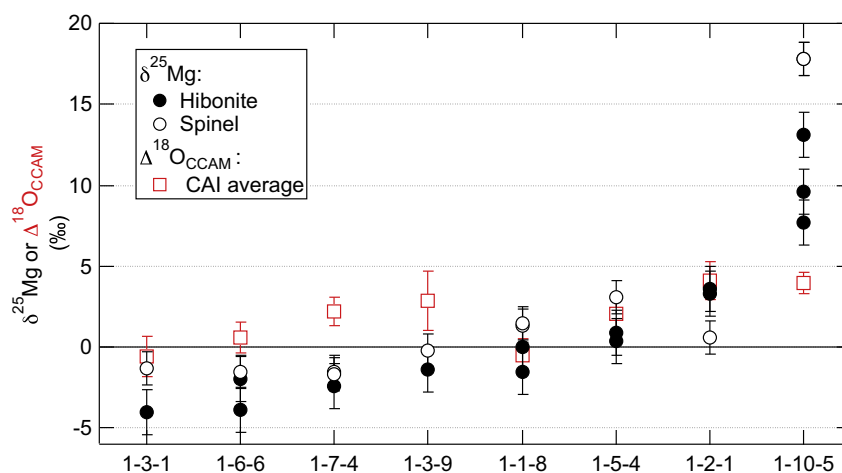

Fig. 7. Possible mass-dependent variations in magnesium (individual analyses, black circles) and oxygen (expressed as $\Delta^{18}O_{CCAM}$, see text; data corresponds to CAI averages, red open squares). Both spinel and hibonite analyses show clear variations in $\delta^{25}Mg$. No clear relationship between oxygen and magnesium isotopic effects is apparent. Uncertainties for $\delta^{25}Mg$ reflect measurement uncertainties (2σ) as well as an estimated 1‰ bias that may have been introduced by the unknown magnesium isotopic composition of the terrestrial mineral standards (see text).

combined with the elevated intercept ($\delta^{26}Mg_0^*$) of the isochron defined by SHIB 1-3-9 (Figs. 4, 5d) is consistent with internal resetting of the ^{26}Al–^{26}Mg system approximately 0.7 Ma after formation of a refractory precursor with a canonical abundance of ^{26}Al. Perhaps this occurred by remelting. The origin of $^{26}Al/^{27}Al$ variations is further discussed in Section 4.4.

The internal and multi-CAI mineral isochrons show no evidence for initial magnesium isotopic heterogeneity (Table 4) at a level that would significantly affect the $^{26}Al/^{27}Al$ ratios inferred from model isochrons. For CAIs that incorporated ^{26}Al, initial magnesium isotopic heterogeneity would be reflected in variations in the isochron intercept, i.e., $\delta^{26}Mg_0^*$. While some of the internal isochrons have positive $\delta^{26}Mg_0^*$ values, the magnitudes are small and could be a result of reprocessing of refractory precursors while ^{26}Al was still alive. If the samples studied here represent the larger population of SHIBs, their lack of large $\delta^{26}Mg_0^*$ variation suggests that formation with a normal initial magnesium isotopic composition is a good approximation for SHIB model isochrons.

A comparison of $^{26}Al/^{27}Al$ ratios obtained from internal and model isochrons suggests that the two approaches yield different distributions. The most precise model $^{26}Al/^{27}Al$ ratios ($N = 34$) show a multi-modal distribution and cover the full range from $\sim(0.5$–$6) \times 10^{-5}$ (Liu et al., 2012). In contrast, our internal isochrons yield high $^{26}Al/^{27}Al$ ratios close to the canonical ratio for seven of eight SHIBs, and only one internal isochron has a clearly resolved lower ratio. Differences in the distributions of $^{26}Al/^{27}Al$ ratios are expected if internal and model isochrons correspond to different events. If model isochrons correspond to true bulk isochrons, they may date gas–solid fractionation

(e.g., condensation), while internal isochrons could date a later event that internally redistributed magnesium and aluminum isotopes (e.g., melting). In turn, internal isochrons would generally be expected to yield lower $^{26}Al/^{27}Al$ ratios (on average) than bulk isochrons. However, the opposite is observed (model and internal isochrons yield averages of 4.1×10^{-5} vs. 4.5×10^{-5} for, respectively). Therefore, it may be possible that the eight SHIBs studied for ^{26}Al–^{26}Mg are not a representative sample. However, we note that 29 of the 34 SHIBs studied by Liu et al. (2012) agree with the ratio inferred from our multi-CAI mineral isochron of $(4.8 \pm 0.1) \times 10^{-5}$ within 2σ uncertainty. Of the remaining five SHIBs, four agree with the lower ratio of $(2.5 \pm 0.7) \times 10^{-5}$ inferred from the internal isochron of SHIB 1-3-9. Based on this work, $^{26}Al/^{27}Al$ ratios established from bulk isochrons cannot be rejected, but additional work is required to evaluate whether internal isochrons yield a different distribution of $^{26}Al/^{27}Al$ ratios.

4.2.3. Calcium and titanium isotopes

If present, mass-dependent fractionation effects in calcium and titanium are small in SHIBs. SHIB 1-5-4 is the only sample with mass fractionation effects in both calcium and titanium that are resolved beyond 3σ (heavy in both titanium and calcium by 1–2‰ amu^{-1}). However, as noted in Section 2.5.3, post-SIMS SEM work showed a cavity in the analysis spot, which could have introduced additional mass-dependent fractionation that was unaccounted for by sample standard bracketing. SHIB 1-3-7 may be slightly enriched in heavy titanium isotopes, but is only marginally resolved beyond 3σ. The other three SHIBs show no clear evidence for mass-dependent fractionation of calcium and titanium isotopes. Therefore, it appears that the studied
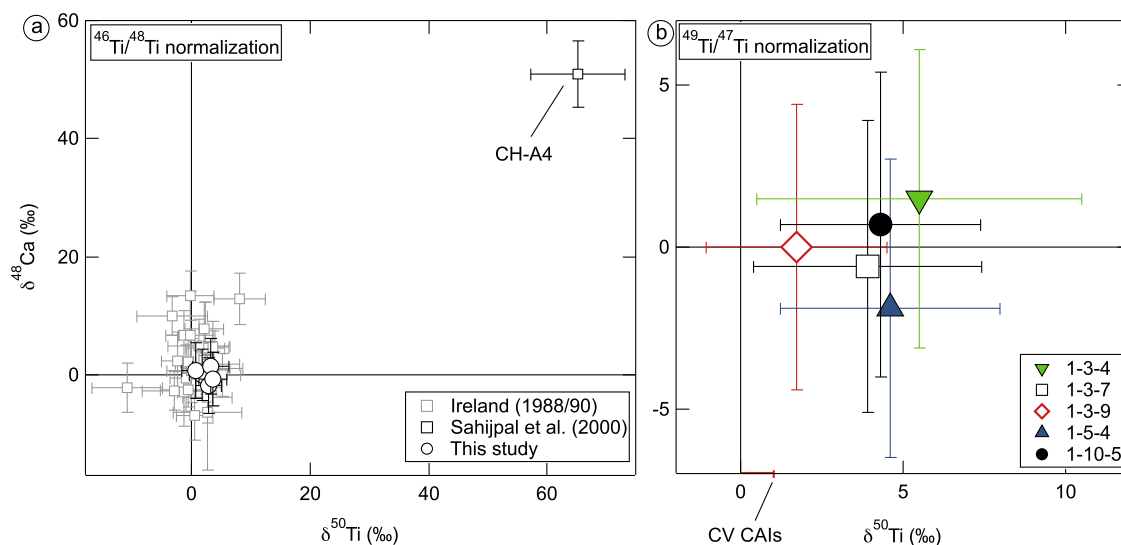

Fig. 8. Comparison of $\delta^{48}Ca$ and $\delta^{50}Ti$ values for five SHIBs with previous studies of CAIs in two different normalizations for titanium isotopes. (a) The five analyzed SHIBs fall inside the cluster defined by SHIBs studied by Ireland (1988 & 1990). SHIB CH-A4 studied by Sahijpal et al. (2000) is clearly distinct from other SHIBs. (b) All five studied SHIBs lack resolvable anomalies in ^{48}Ca. Four SHIBs have marginally resolved excesses in ^{50}Ti beyond the 2σ uncertainty in $^{49}Ti/^{47}Ti$ normalization, but SHIB 1-3-9 has no resolvable anomaly in ^{50}Ti. All SHIBs are within uncertainty of the maximum $\delta^{50}Ti$ found in CV CAIs (red bar on $\delta^{50}Ti$ axis; Trinquier et al., 2009). Plotted uncertainties are 2σ. (For interpretation of the references to colour in this figure legend, the reader is referred to the web version of this article.)

SHIBs are either heavy or normal in calcium and titanium within the precision achieved in this study. In contrast, many CV chondrite CAIs that have been analyzed using the double-spike technique are isotopically light in calcium isotopes (F_{Ca} as low as $\sim$–4‰/amu; Niederer and Papanastassiou, 1984; Huang et al., 2012). While this contrast could indicate differences in the formation history of these CAIs, the majority of studied CV chondrite CAIs have F_{Ca} values between 0 and −1‰/amu, which is comparable to the uncertainty achieved by the SIMS measurements presented here and would thus be hard to recognize.

None of the five SHIBs studied for calcium and titanium isotopes show resolvable anomalies beyond the 3σ level (Table 5 and Fig. 8). For comparison, many PLAC-like CAIs analyzed in the same session have anomalies in calcium and/or titanium isotopes resolved beyond 3σ, with $\delta^{50}Ti$ and $\delta^{48}Ca$ ranges of $\sim$240‰ ($^{46}Ti/^{48}Ti$ normalization) and $\sim$140‰, respectively (Kööp et al., 2014b), which is in agreement with previous studies of similar objects (Ireland, 1988, 1990; Liu et al., 2009a). This result suggests that the studied SHIBs formed in a well-mixed reservoir, after the large calcium and titanium anomalies that characterize PLAC-like CAIs had been diluted within the CAI formation region. Alternative interpretations such as homogenization by reprocessing and exchange of SHIB precursors with the surrounding gas are less likely for calcium and titanium than for oxygen or even magnesium, as these are highly refractory elements that would not have been present in the gas phase unless SHIBs were reprocessed at very high temperatures. If present, anomalies in ^{50}Ti appear to be positive, which is similar to the small-scale anomalies found in CV chondrite CAIs, and all anomalies are within 2σ uncertainty of the range found in CV chondrite CAIs (e.g., Trinquier et al., 2009; Fig. 8). This could suggest that both types of CAIs formed in reservoirs that had experienced similar degrees of dilution of nucleosynthetic anomalies in refractory elements by mixing and/or thermal processes. However, higher precision analyses of a larger number of SHIBs would be desirable to fully assess the degree of heterogeneity in SHIBs.

The lack of clearly defined anomalies in the five studied SHIBs in contrast to previous studies, which found a larger spread in $\delta^{48}Ca$ (Fig. 8a). In addition, previous studies have shown that approximately a third of these CAIs have anomalies in ^{50}Ti beyond the 3σ level (Ireland, 1988, 1990; Fahey et al., 1987; Sahijpal et al., 2000; Liu et al., 2009a). However, anomalies in these SHIBs are typically within 10‰ of the terrestrial value, and are thus smaller than those in PLACs and PLAC-like CAIs. In contrast, SHIBs 7-170 and CH-A4 studied by Ireland (1988) and Sahijpal et al. (2000), respectively, have large ^{50}Ti anomalies in excess of 10‰ (the latter is plotted in Fig. 8a). But these SHIBs have no or only marginally resolved radiogenic ^{26}Mg excesses (Ireland, 1988; Sahijpal et al., 2000) and 7-170 also shows a hint of a ^{16}O-depletion ($\Delta^{17}O$ of −18.6 ± 3.5‰; Ireland et al., 1992) relative to the SHIBs presented here; no oxygen isotope results have been reported for CH-A4. As such, 7-170 and CH-A4 could belong to a different isotopic population, for example to the PLAC-like CAIs, which are ^{26}Al-depleted and show increasing degrees of isotopic heterogeneity in refractory elements with increasing $\Delta^{17}O$ (Kööp et al., 2014b, 2015). The existence of these SHIBs demonstrates the importance of performing multielement isotopic studies on these objects instead of inferring isotopic properties of hibonite-rich CAIs from their mineralogy and morphology. To evaluate how the magnitudes of anomalies in SHIBs with uniform oxygen isotopic compositions compare to other types of CAIs, it is necessary to expand multielement isotopic studies to a larger number of SHIBs.

4.3. Relationship between mass-dependent isotope fractionation effects in SHIBs

The consistency between mass-dependent signatures in magnesium, calcium and titanium can best be evaluated in SHIBs for which all three isotopic systems have been studied (i.e., samples 1-3-9, 1-5-4 and 1-10-5). 1-3-9 and 1-10-5 lack clear evidence for calcium and titanium isotopic fractionation (beyond 3σ), which is consistent with the magnesium isotopic fractionation in these CAIs ($\delta^{25}Mg \sim 0$ in 1-3-9 and $\sim$8–18‰ in 1-10-5). If caused by melt evaporation, no significant loss (and thus no significant fractionation) of refractory elements like calcium and titanium would be expected based on these low degrees fractionation in magnesium (as modeled by Simon and DePaolo, 2010, for calcium and magnesium isotopes). Similar to 1-3-9 and 1-10-5, no resolvable fractionation in calcium and titanium isotopes would be expected for SHIB 1-5-4, which shows a low degree of fractionation in magnesium ($\delta^{25}Mg < 5$‰). In contrast, 1-5-4 appears to be enriched in heavy calcium and titanium isotopes by $\sim$1–2‰ amu^{-1}. As discussed in Section 4.2.3, this could be the result of insufficient correction for instrumental fractionation for this CAI. However, intrinsic fractionation cannot be excluded based on the available data, and would require a multistage formation history (e.g., evaporation of calcium and titanium from a melt, followed by processes that allowed for acquisition of isotopically normal or slightly heavy magnesium).

Based on the eight SHIBs studied for both oxygen and magnesium isotopes, no clear link is apparent between mass-dependent effects in magnesium and oxygen, similar to many other CAIs (e.g., Krot et al., 2008). To assess mass-dependent variation in oxygen isotopes, we define the $\Delta^{18}O_{CCAM}$ value, which is a measure of the deviation from the CCAM line in $\delta^{18}O$ ($\Delta^{18}O_{CCAM} = \delta^{18}O + (\Delta^{17}O-$Intercept$_{CCAM})/($Slope$_{MFL}-$Slope$_{CCAM})$, MFL = mass fractionation line). Under the assumption that all deviations from the CCAM line result from mass-dependent fractionation, $\Delta^{18}O_{CCAM}$ values can be directly compared to $\delta^{18}O$ values from experimental melt evaporation studies (e.g., Mendybaev et al., 2013). Based on CAI liquid evaporation experiments, mass-dependent fractionation should result in effects of similar magnitudes in $\delta^{18}O$ and $\delta^{25}Mg$ values (Mendybaev et al., 2013). In contrast, the $\Delta^{18}O_{CCAM}$ range defined by the eight studied SHIBs is approximately half of the $\delta^{25}Mg$ range (the $\Delta^{18}O_{CCAM}$ ranges are $\sim$9‰ and $\sim$8‰ for spot analyses of hibonite and spinel, respectively, compared to $\delta^{25}Mg$ ranges of $\sim$20‰ for spinel and

~17‰ for hibonite). However, the dataset for magnesium is small and only one SHIB is primarily responsible for the larger range in δ^{25}Mg (1-10-5). δ^{25}Mg values of the other seven SHIBs (range of ~5‰ for spinel, ~8‰ for hibonite) are more consistent with the $\Delta^{18}O_{CCAM}$ range, however, no clear relationship is observed between δ^{25}Mg and $\Delta^{18}O_{CCAM}$ for these seven SHIBs either (Fig. 7).

A clear deviation from the relationship between δ^{18}O and δ^{25}Mg found by Mendybaev et al. (2013) is shown by SHIB 1-10-5, which has a more complex mass-fractionation pattern than other SHIBs. As illustrated in Fig. 7, δ^{25}Mg values in spinel are higher than those in hibonite and the magnitude of δ^{25}Mg values in hibonite decreases with distance from the spinel grain and correlates with ^{27}Al/^{24}Mg (Fig. 9a and b). The magnesium isotopic data can be explained if this SHIB formed from a melt that had become isotopically heavy in magnesium due to considerable evaporative loss (e.g., Mendybaev et al., 2013). After crystallization of isotopically heavy spinel, MgO-poor, isotopically heavy hibonite may have nucleated on the spinel
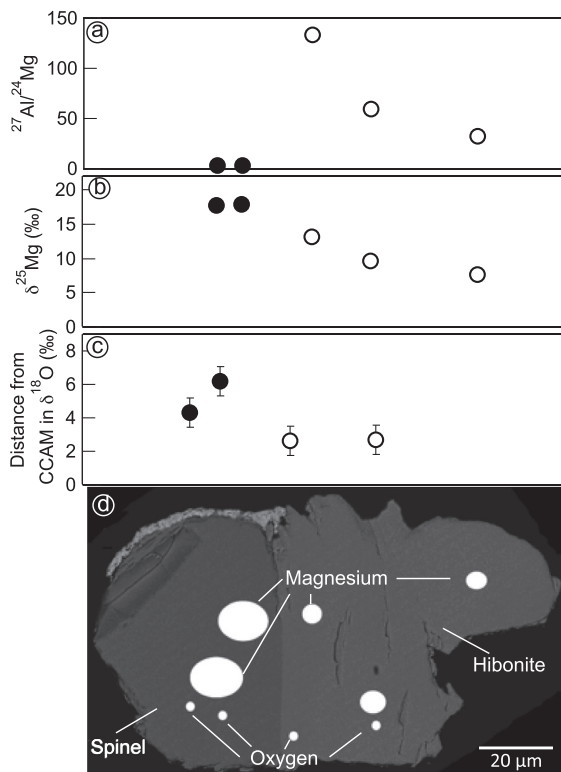
Fig. 9. Elemental and isotopic zonation in SHIB 1-10-5, the *x*-axis corresponds to analysis locations in the BSE image in (d). (a) The hibonite grain is zoned with respect to MgO, i.e., its MgO contents increase with distance from the spinel grain. (b) The spinel grain in SHIB 1-10-5 is fractionated in magnesium by >15‰ amu^{-1}, fractionation in hibonite is smaller and decreases with distance from the spinel grain. (c) Using the CCAM line as a reference, both spinel and hibonite appear to be isotopically heavy in oxygen, but heavy isotope enrichment is less pronounced than in magnesium. (d) BSE image of SHIB-1-10-5, white ellipses indicate locations and relative sizes of analysis spots. 2σ uncertainties are plotted for all data, but are smaller than symbol sizes for (a) and (b).

grain. Recondensation of magnesium into the melt while hibonite continued to crystallize could then have resulted in the increasing MgO contents and smaller heavy isotope enrichments in crystallizing hibonite (Fig. 9a and b). While spinel may also be slightly heavier in oxygen isotopes than hibonite in this CAI, the range of mass-dependent effects in oxygen is clearly smaller than that in magnesium ($\Delta^{18}O_{CCAM}$ range of ~4‰, compared to a δ^{25}Mg range of ~10‰). Efficient oxygen isotopic exchange between the SHIB melt and the gas phase may be required to explain the lack of comparable zoning in oxygen isotopes.

4.4. Timing of SHIB formation and relationships to other types of CAIs

Based on the newly obtained isotopic data for a large number of SHIBs, we infer that the SHIB formation reservoir was significantly more homogeneous in its isotopic properties than previously hypothesized. In terms of their oxygen isotopic uniformity (average Δ^{17}O of –23.4 ± 1.1‰) and their ^{26}Al–^{26}Mg characteristics, we find that SHIBs bear a greater resemblance to CR CAIs and Acfer 094 CAIs than to PLAC-like CAIs. Whether this is also the case for calcium and titanium isotopes needs to be evaluated in future studies that include SHIBs and other types of CAIs.

Based on model isochrons of SHIBs, it has been suggested that their variable initial ^{26}Al/^{27}Al ratios could be the result of a formation during admixing of ^{26}Al into the nebula (Liu et al., 2012). In particular, the distribution of model ^{26}Al/^{27}Al ratios was found to be most consistent with continuous formation in a fairly well-mixed reservoir in which the ^{26}Al/^{27}Al ratio was increasing. If isotopic anomalies in the CAI formation region were erased over time by mixing processes, this early formation scenario may be supported by the range of ^{48}Ca and ^{50}Ti anomalies in SHIBs, which is intermediate between the anomalous, ^{26}Al-depleted PLACs and the ^{26}Al-rich, more isotopically uniform regular CAIs (e.g., Ireland, 1988; Sahijpal et al., 2000; Liu et al., 2009a). The chronologic sequence suggested by this scenario would be that PLAC formation was followed by an extended period of SHIB formation, which was followed by or overlapped with the formation of regular CAIs. Our internal isochrons are consistent with a certain degree of variability in the ^{26}Al/^{27}Al ratios of SHIBs, as CAI 1-3-9 deviates from the well-defined multi-CAI mineral isochron. This is consistent with an early, extended SHIB formation period during ^{26}Al admixture, as suggested by Liu et al. (2012). However, CAI 1-3-9 has no resolved anomalies in calcium and titanium isotopes and its Δ^{17}O is indistinguishable from other SHIBs, suggesting that it formed in an evolved isotopic reservoir. This new data may indicate that either subcanonical ^{26}Al/^{27}Al ratios in SHIBs are due to reprocessing of precursors that formed with a canonical abundance of ^{26}Al, or that the CAI formation region was already highly homogenized in oxygen, calcium and titanium isotopes when ^{26}Al was still heterogeneously distributed. Below, both scenarios are evaluated. For this, the initial ^{26}Al/^{27}Al ratio inferred from the multi-CAI mineral isochron is assumed to be accurate

(i.e., truly subcanonical). However, we note again that due to the lack of an appropriate hibonite standard, a canonical incorporation of ^{26}Al and thus a contemporaneous formation with CV CAIs cannot be excluded for seven of the eight studied SHIBs (see Appendix).

A comparison with CV CAIs shows that the high, yet subcanonical ^{26}Al/^{27}Al ratio in seven SHIBs could reflect remelting after partial decay of ^{26}Al. Similar to SHIBs, CV CAIs have been interpreted to have formed in a ^{16}O-rich oxygen isotopic reservoir with an average Δ^{17}O of $\sim$– 23‰ (e.g., Bullock et al., 2012). Bulk isochrons of CV CAIs suggest that they formed with a canonical ratio of $(5.23 \pm 0.13) \times 10^{-5}$ (Jacobsen et al., 2008; Larsen et al., 2011). Similarly high values have been inferred from internal isochrons of two unmelted CV CAIs, but for melted CAIs, internal isochrons yield a range of initial ratios (i.e., $\sim 4.2 \times 10^{-5}$ to 5.2×10^{-5}; MacPherson et al., 2012), suggesting that CAI formation processes and/or high-temperature processing occurred for $\sim$0.2–0.3 Ma after formation of CAIs with canonical ^{26}Al. The average ^{26}Al/^{27}Al ratio inferred from the multi-SHIB mineral isochron of 4.8×10^{-5} falls into the range defined by melted CV CAIs and thus suggests that this ratio, if truly subcanonical, may be a result of reprocessing rather than an early formation while ^{26}Al was being admixed.

The lack of clearly resolved anomalies in oxygen, calcium, and titanium isotopes seems consistent with both scenarios (i.e., formation before or after canonical CAIs) for these seven SHIBs. If the ^{26}Al/^{27}Al ratio of $\sim 4.8 \times 10^{-5}$ reflects decay, isotopic properties similar to those found in CV CAIs would be expected, i.e., anomalies in calcium and titanium that would be unresolvable with the precision achieved in this study and uniform oxygen isotopic compositions. Alternatively, if the SHIBs formed during admixture of ^{26}Al, the uniformly high abundance of this SLR in seven of the eight studied SHIBs (>90% of the canonical value) suggests that the CAI formation region was close to achieving a homogeneous distribution of ^{26}Al. Since we expect that the processes that homogenized ^{26}Al would also have resulted in dilution of other nucleosynthetic signatures, the seven SHIBs should be significantly more isotopically uniform than the ^{26}Al-free PLAC-like CAIs. However, if the low ^{26}Al/^{27}Al ratio in SHIB 1-3-9 was due to an early formation during ^{26}Al admixture and the larger range of anomalies in ^{48}Ca and ^{50}Ti established in previous studies of SHIBs was accurate, resolvable anomalies in calcium, titanium (and possibly also oxygen) would be expected in this SHIB. In this view, the nonzero intercept of the isochron for 1-3-9 (Fig. 5d) could be interpreted as magnesium isotopic heterogeneity. However, this SHIB shows no resolvable anomalies in calcium and titanium isotopes (Fig. 8b), and falls into the SHIB cluster in oxygen isotopes (Fig. 3), suggesting that this CAI formed in a highly homogenized reservoir. As argued in Section 4.2.2, the nonzero intercept and shallow slope could instead indicate thermal reprocessing of a refractory precursor with a canonical ratio approximately 0.7 Ma after its formation. The low initial ^{26}Al/^{27}Al ratio of $(2.5 \pm 0.7) \times 10^{-5}$ found in SHIB 1-3-9 is in agreement with a low value found in the Type C mineralogy of a composite CV CAI, (2.8

$\pm 0.8) \times 10^{-5}$ (MacPherson et al., 2012). But while the low-temperature assemblage of this part of the CAI is consistent with having formed during remelting in a chondrule forming region, SHIB 1-3-9 shows no evidence for such low-temperature phases and its Δ^{17}O value of -23.7 ± 1.0‰ suggests that reprocessing occurred in a reservoir that was as enriched in ^{16}O as the original SHIB formation reservoir. This interpretation is supported by an Acfer 094 CAI, which contains secondary anorthite that likely formed through interaction with the solar nebula gas (Ushikubo et al., 2011). The ^{26}Al/^{27}Al ratio in the anorthite is even lower than the ratio found in 1-3-9, but it is ^{16}O-rich, which suggests that a ^{16}O-rich gaseous reservoir existed in the solar nebula for up to $\sim$2.3 Ma (based on the ^{26}Al/^{27}Al ratio of $(5.38 \pm 0.52) \times 10^{-6}$; Ushikubo et al., 2011).

Finally, it should be noted that resetting of the ^{26}Al–^{26}Mg system may also account for the potentially supracanonical ^{26}Al/^{27}Al values that have been inferred from model isochrons for SHIBs in previous studies (Ireland 1990; Liu et al., 2009a, 2012). If SIMS analyses of SHIBs are true bulk analyses and SHIBs behaved as closed systems, resetting and/or remelting should not affect initial ^{26}Al/^{27}Al ratios. However, as SIMS analyses only consume a fraction of the CAI as part of it is removed during polishing and sampling depth is limited, they may be susceptible to unrepresentative sampling. Unrepresentative sampling of an internally reset CAI would yield coordinates that fall on the internal isochron, and a regression of such data through normal magnesium could yield both sub- and supracanonical ^{26}Al/^{27}Al ratios. This can be illustrated using our data for SHIB 1-3-9 as an example. The most extreme cases for unrepresentative sampling would be analyses that are purely spinel or purely hibonite. Model isochrons constructed for the hibonite and spinel analyses would yield sub- and supracanonical ^{26}Al/^{27}Al ratios (i.e., $\sim 2.8 \times 10^{-5}$ and $\sim 6.7 \times 10^{-5}$), respectively. In order to account for the scatter in ^{26}Al/^{27}Al ratios inferred from model isochrons, a considerable number of SHIBs would have to have been reset.

Therefore, it can be concluded that the observed range in ^{26}Al/^{27}Al ratios inferred from both previous model and our internal isochrons of SHIBs could be consistent with high temperature processing, e.g., remelting, of refractory precursors that formed with approximately canonical ^{26}Al/^{27}Al ratios. This interpretation is supported by the uniform oxygen, calcium, and titanium isotopic character of the studied inclusions, which suggests formation in a reservoir that had achieved a similar degree of homogeneity as the CV CAI formation reservoir. Alternatively, if SHIBs recorded the mostly unsampled epoch of ^{26}Al admixture into the CAI formation region, as suggested by Liu et al. (2012), the data would suggest a high degree of isotopic homogenization in oxygen and refractory elements while ^{26}Al was still heterogeneously distributed in the solar nebula.

5. CONCLUSIONS

We obtained high precision oxygen isotopic analyses in a large number of SHIBs, with a spatial resolution sufficiently high to allow efficient measurement of individual,

primary phases. The results show that SHIBs formed with a uniform $\Delta^{17}O$ of approximately –23‰. This observation is in contrast to previous studies of similar samples (Liu et al., 2009a), but in excellent agreement with studies of primitive CAIs from other chondrite groups (Makide et al., 2009; Ushikubo et al., 2011; Bullock et al., 2012), which suggests formation in similar isotopic reservoir(s) with a uniform distribution of oxygen isotopes.

Regarding calcium and titanium isotopes, we found no resolvable anomalies beyond the 3σ level in the five SHIBs analyzed. However, the average $\delta^{50}Ti$ value of these SHIBs hints at a slight enrichment, comparable to CV chondrite CAIs. While the sample set studied for calcium and titanium isotopes is limited, the data may suggest that calcium and titanium anomalies were highly diluted when SHIBs with a $\Delta^{17}O$ of approximately –23‰ formed.

Internal $^{26}Al–^{26}Mg$ isochrons for eight SHIBs were established. We found that seven of these are consistent with high, yet possibly slightly subcanonical $^{26}Al/^{27}Al$ ratios and show no significant anomalies in magnesium isotopes. The remaining SHIB appears to have formed with a significantly lower $^{26}Al/^{27}Al$ ratio ($\sim 2.5 \times 10^{-5}$), confirming variation in $^{26}Al/^{27}Al$ ratios inferred from one-point model isochrons in previous studies of similar objects. The slope and intercept of the isochron are consistent with a late reprocessing event of the refractory precursor of this SHIB after significant ^{26}Al decay, which would imply that high temperature events still affected some CAIs 0.7 Ma after formation of CAIs with canonical ratios. Since the $\Delta^{17}O$ value of this SHIB is consistent with other SHIBs, this result would further suggest that an ^{16}O-rich gaseous reservoir still existed in the nebula ~ 0.7 Ma after canonical CAIs formed.

While we cannot exclude the possibility that subcanonical $^{26}Al/^{27}Al$ ratios inferred for SHIBs are a result of early formation during admixture of ^{26}Al, we see no support for this scenario in our dataset. Since isotopic anomalies are expected to be diluted during progressive admixture of ^{26}Al, one might expect to see a negative correlation between ^{26}Al abundance and the magnitude of nucleosynthetic anomalies. In contrast, no clearly resolvable anomalies were found in any of the analyzed SHIBs, including the most ^{26}Al-depleted SHIB 1-3-9. In addition, formation during ^{26}Al injection could have resulted in a significant number of SHIBs with supracanonical ratios. While previous studies report supracanonical ratios from SHIB model isochrons, these are primarily inferred from analyses with low $^{27}Al/^{24}Mg$ and could be explained by resetting of the $^{26}Al–^{26}Mg$ system, for example by remelting. Therefore, we tentatively conclude that SHIBs are unlikely to be recorders of ^{26}Al admixture into the Solar System and that in terms of their isotopic properties, they more closely resemble primitive CAIs from other chondrite groups than the anomalous PLAC-like CAIs.

APPENDIX A. SUPPLEMENTARY DATA

Supplementary data associated with this article can be found, in the online version, at http://dx.doi.org/10.1016/j.gca.2016.04.018.

REFERENCES

Amari S., Lewis R. S. and Anders E. (1994) Interstellar grains in meteorites. I – isolation of SiC, graphite, and diamond; size distributions of SiC and graphite. II – SiC and its noble gases. *Geochim. Cosmochim. Acta* **58**, 459–470.

Amelin Y., Krot A. N., Hutcheon I. D. and Ulyanov A. A. (2002) Lead isotopic ages of chondrules and calcium–aluminum-rich inclusions. *Science* **297**, 1678–1683.

Bodénan J.-D., Starkey N. A., Russell S. S., Wright I. P. and Franchi I. A. (2014) An oxygen isotope study of Wark–Lovering rims on type A CAIs in primitive carbonaceous chondrites. *Earth Planet. Sci. Lett.* **401**, 327–336.

Bullock E. S., MacPherson G. J., Nagashima K., Krot A. N., Petaev M. I., Jacobsen S. B. and Ulyanov A. A. (2012) Forsterite-bearing type B refractory inclusions from CV3 chondrites: from aggregates to volatilized melt droplets. *Meteorit. Planet. Sci.* **47**, 2128–2147.

Catanzaro E. J., Murphy T. J., Garner E. L. and Shields W. R. (1966) Absolute isotopic abundance ratios and atomic weights of magnesium. *J. Res. Natl. Bur. Stand.* **70a**, 453–458.

Clayton R. N., Onuma N., Grossman L. and Mayeda T. K. (1977) Distribution of the presolar component in Allende and other carbonaceous chondrites. *Earth Planet. Sci. Lett.* **34**, 209–224.

Connelly J. N., Bizzarro M., Krot A. N., Nordlund Å., Wielandt D. and Ivanova M. A. (2012) The absolute chronology and thermal processing of solids in the solar protoplanetary disk. *Science* **338**, 651–655.

Davis A. M., Richter F. M., Mendybaev R. A., Janney P. E., Wadhwa M. and McKeegan K. D. (2005) Isotopic mass fractionation laws and the initial Solar System $^{26}Al/^{27}Al$ ratio. *Lunar Planet. Sci.* **36**, 2334.

Davis A. M., Richter F. M., Mendybaev R. A., Janney P. E., Wadhwa M. and McKeegan K. D. (2015) Isotopic mass fractionation laws for magnesium and their effects on $^{26}Al–^{26}Mg$ systematics in Solar System materials. *Geochim. Cosmochim. Acta* **158**, 245–261.

Fahey A. J. (1998) Measurements of dead time and characterization of ion counting systems for mass spectrometry. *Rev. Sci. Instrum.* **69**, 1282–1288.

Fahey A. J., Goswami J. N., McKeegan K. D. and Zinner E. (1987) ^{26}Al, ^{244}Pu, ^{50}Ti, REE, and trace element abundances in

hibonite grains from CM and CV meteorites. *Geochim. Cosmochim. Acta* **51**, 329–350.

Heck P. R., Ushikubo T., Schmitz B., Kita N. T., Spicuzza M. J. and Valley J. W. (2010) A single asteroidal source for extraterrestrial Ordovician chromite grains from Sweden and China: high-precision oxygen three-isotope SIMS analysis. *Geochim. Cosmochim. Acta* **74**, 497–509.

Huang S., Farkaš J., Yu G., Petaev M. I. and Jacobsen S. B. (2012) Calcium isotopic ratios and rare earth element abundances in refractory inclusions from the Allende CV3 chondrite. *Geochim. Cosmochim. Acta* **77**, 252–265.

Ireland T. R. (1988) Correlated morphological, chemical, and isotopic characteristics of hibonites from the Murchison carbonaceous chondrite. *Geochim. Cosmochim. Acta* **52**, 2827–2839.

Ireland T. R. (1990) Presolar isotopic and chemical signatures in hibonite-bearing refractory inclusions from the Murchison carbonaceous chondrite. *Geochim. Cosmochim. Acta* **54**, 3219–3237.

Ireland T. R., Zinner E. K., Fahey A. J. and Esat T. M. (1992) Evidence for distillation in the formation of HAL and related hibonite inclusions. *Geochim. Cosmochim. Acta* **56**, 2503–2520.

Itoh S. and Yurimoto H. (2003) Contemporaneous formation of chondrules and refractory inclusions in the early solar system. *Nature* **423**, 728–731.

Jacobsen B., Yin Q., Moynier F., Amelin Y., Krot A. N., Nagashima K., Hutcheon I. D. and Palme H. (2008) $^{26}Al–^{26}Mg$ and $^{207}Pb–^{206}Pb$ systematics of Allende CAIs: canonical solar initial $^{26}Al/ ^{27}Al$ ratio reinstated. *Earth Planet. Sci. Lett.* **272**, 353–364.

Kita N. T., Nagahara H., Tachibana S., Tomomura S., Spicuzza M. J., Fournelle J. H. and Valley J. W. (2010) High precision SIMS oxygen three isotope study of chondrules in LL3 chondrites: role of ambient gas during chondrule formation. *Geochim. Cosmochim. Acta* **74**, 6610–6635.

Kita N. T., Ushikubo T., Fu B. and Valley J. W. (2009) High precision SIMS oxygen isotope analysis and the effect of sample topography. *Chem. Geol.* **264**, 43–57.

Kita N. T., Ushikubo T., Knight K. B., Mendybaev R. A., Davis A. M., Richter F. M. and Fournelle J. H. (2012) Internal $^{26}Al–^{26}Mg$ isotope systematics of a Type B CAI: remelting of refractory precursor solids. *Geochim. Cosmochim. Acta* **86**, 37–51.

Kööp L., Davis A. M., Kita N. T., Nakashima D., Tenner T. J., Krot A. N., Park C., Nagashima K. and Heck P. R. (2015) ^{26}Al-depletions in anomalous and solar PLAC-like CAIs suggest high degrees of processing in the early Solar Nebula. *Meteor. Planet. Sci. Suppl.* **50**, 5225.

Kööp L., Heck P. R., Nakashima D., Kita N. T. and Davis A. M. (2014a) Precise oxygen isotope measurements reveal difference between single hibonite crystals and spinel-hibonite inclusions from CM chondrites. *Lunar Planet. Sci.* **45**, 2508.

Kööp L., Park C., Krot A. N., Nagashima K., Nakashima D., Kita N. T., Heck P. R. and Davis A. M. (2014b) Ca and Ti isotopes in platy hibonite crystals support the existence of an 16O-depleted reservoir in the early Solar System. *Meteor. Planet. Sci. Suppl.* **49**, 5384.

Krot A. N., Nagashima K., Bizzarro M., Huss G. R., Davis A. M., Meyer B. S. and Ulyanov A. A. (2008) Multiple generations of refractory inclusions in the metal-rich carbonaceous chondrites Acfer 182/214 and Isheyevo. *Astrophys. J.* **672**, 713–721.

Krot A. N., Makide K., Nagashima K., Huss G. R., Ogliore R. C., Ciesla F. J., Yang L., Hellebrand E. and Gaidos E. (2012) Heterogeneous distribution of ^{26}Al at the birth of the solar system: evidence from refractory grains and inclusions. *Meteorit. Planet. Sci.* **47**, 1948–1979.

Larsen K., Trinquier A., Paton C., Schiller M., Wielandt D., Ivanova M. A., Connelly J. N., Nordlund Å., Krot A. N. and Bizzaro M. (2011) Evidence for magnesium isotope heterogeneity in the solar protoplanetary disk. *Astrophys. J.* **735**, L37 (7 pp).

Lee T., Papanastassiou D. A. and Wasserburg G. J. (1976) Demonstration of ^{26}Mg excess in Allende and evidence for ^{26}Al. *Geophys. Res. Lett.* **3**, 109–112.

Liu M.-C., Chaussidon M., Göpel C. and Lee T. (2012) A heterogeneous solar nebula as sampled by CM hibonite grains. *Earth Planet. Sci. Lett.* **327**, 75–83.

Liu M.-C., McKeegan K. D., Goswami J. N., Marhas K. K., Sahijpal S., Ireland T. R. and Davis A. M. (2009a) Isotopic records in CM hibonites: implications for timescales of mixing of isotope reservoirs in the solar nebula. *Geochim. Cosmochim. Acta* **73**, 5051–5079.

Liu M.-C., Nittler L. R., Alexander C. M. O'D. and Lee T. (2009b) A search for internal ^{26}Al isochrons in CM hibonite. *Lunar Planet. Sci.* **40**, 1739.

Ludwig K. (2003). ISOPLOT: A geochronological toolkit for Microsoft Excel 3.00. Berkeley Geochronology Center Special Publication No. 4, 2455 Ridge Road, Berkeley CA 94709.

Luu T.-H., Chaussidon M., Mishra R. K., Rollion-Bard C., Villeneuve J., Srinivasan G. and Birck J.-L. (2013) High precision Mg isotope measurements of meteoritic samples by secondary ion mass spectrometry. *J. Anal. At. Spectrom.* **28**, 67–76.

MacPherson G. J., Kita N. T., Ushikubo T., Bullock E. S. and Davis A. M. (2012) Well-resolved variations in the formation ages for Ca–Al-rich inclusions in the early solar system. *Earth Planet. Sci. Lett.* **331**, 43–54.

MacPherson G. J., Matthews M. B., Tanaka T., Olsen E. and Grossman L. (1980) Refractory inclusions in Murchison: recovery and mineralogical description. *Lunar Planet. Sci.* **11**, 660–662.

Makide K., Nagashima K., Krot A. N., Huss G. R., Hutcheon I. D. and Bischoff A. (2009) Oxygen- and magnesium-isotope compositions of calcium–aluminum-rich inclusions from CR2 carbonaceous chondrites. *Geochim. Cosmochim. Acta* **73**, 5018–5050.

McKeegan K. D., Kallio A. P. A., Heber V. S., Jarzebinski G., Mao P. H., Coath C. D., Kunihiro T., Wiens R. C., Nordholt J. E., Moses R. W., Reisenfeld D. B., Jurewicz A. J. G. and Burnett D. S. (2011) The oxygen isotopic composition of the Sun inferred from captured solar wind. *Science* **332**, 1528–1532.

Mendybaev R. A., Richter F. M., Georg R. B., Janney P. E., Spicuzza M. J., Davis A. M. and Valley J. W. (2013) Experimental evaporation of Mg- and Si-rich melts: implications for the origin and evolution of FUN CAIs. *Geochim. Cosmochim. Acta* **123**, 368–384.

Nakashima D., Ushikubo T., Gowda R. N., Kita N. T., Valley J. W. and Nagao K. (2011) Ion microprobe analyses of oxygen three-isotope ratios of chondrules from the Sayh al Uhaymir 290 CH chondrite using a multiple-hole disk. *Meteoritics* **46**, 857–874.

Niederer F. R. and Papanastassiou D. A. (1984) Ca isotopes in refractory inclusions. *Geochim. Cosmochim. Acta* **48**, 1279–1293.

Niederer F. R., Papanastassiou D. A. and Wasserburg G. J. (1981) The isotopic composition of titanium in the Allende and Leoville meteorites. *Geochim. Cosmochim. Acta* **45**, 1017–1031.

Park C., Nagashima K., Wasserburg G. J., Papanastassiou D. A., Hutcheon I. D., Davis A. M., Huss G. R., Bizzarro M. and Krot A. N. (2014) Calcium and titanium isotopic compositions of FUN CAIs: implications for their origin. *Lunar Planet. Sci.* **45**, 2656.

Park C., Wakaki S., Sakamoto N., Kobayashi S. and Yurimoto H. (2012) Oxygen isotopic composition of the solar nebula gas inferred from high-precision isotope imaging of melilite crystals in an Allende CAI. *Meteoritics* **47**, 2070–2083.

Richter F. M., Davis A. M., Ebel D. S. and Hashimoto A. (2002) Elemental and isotopic fractionation of Type B calcium-, aluminum-rich inclusions: experiments, theoretical considerations, and constraints on their thermal evolution. *Geochim. Cosmochim. Acta* **66**, 521–540.

Sahijpal S. and Goswami J. N. (1998) Refractory phases in primitive meteorites devoid of ^{26}Al and ^{41}Ca: representative samples of first solar system solids? *Astrophys. J.* **509**, L137–L140.

Sahijpal S., Goswami J. N. and Davis A. M. (2000) K, Mg, Ti and Ca isotopic compositions and refractory trace element abundances in hibonites from CM and CV meteorites: implications for early solar system processes. *Geochim. Cosmochim. Acta* **64**, 1989–2005.

Schwander D., Kööp L., Berg T., Schönhense G., Heck P. R., Davis A. M. and Ott U. (2015) Formation of refractory metal nuggets and their link to the history of CAIs. *Geochim. Cosmochim. Acta* **168**, 70–87.

Simon J. I., Hutcheon I. D., Simon S. B., Matzel J. E. P., Ramon E. C., Weber P. K., Grossman L. and DePaolo D. J. (2011) Oxygen isotope variations at the margin of a CAI records circulation within the solar nebula. *Science* **331**, 1175–1178.

Simon J. I. and DePaolo D. J. (2010) Stable calcium isotopic composition of meteorites and rocky planets. *Earth Planet. Sci. Lett.* **289**, 457–466.

Simon J. I. and Young E. D. (2011) Resetting, errorchrons and the meaning of canonical CAI initial ^{26}Al/^{27}Al values. *Earth Planet. Sci. Lett.* **304**, 468–482.

Simon S. B., Yoneda S., Grossman L. and Davis A. M. (1994) A CaA1$_4$O$_7$-bearing refractory spherule from Murchison: evidence for very high-temperature melting in the solar nebula. *Geochim. Cosmochim. Acta* **58**, 1937–1949.

Trinquier A., Elliott T., Ulfbeck D., Coath C., Krot A. N. and Bizzarro M. (2009) Origin of nucleosynthetic isotope heterogeneity in the solar protoplanetary disk. *Science* **324**, 374.

Ushikubo T., Kimura M., Kita N. T. and Valley J. W. (2012) Primordial oxygen isotope reservoirs of the solar nebula recorded in chondrules in Acfer 094 carbonaceous chondrite. *Geochim. Cosmochim. Acta* **90**, 242–264.

Ushikubo T., Tenner T. J., Hiyagon H. and Kita N. T. (2011) Lifetime of ^{16}O-rich oxygen isotope reservoir in the solar nebula. *LPI Contrib.* **1639**, 9086.

Ushikubo T., Nakashima D., Kimura M., Tenner T. J. and Kita N. T. (2013) Contemporaneous formation of chondrules in distinct oxygen isotope reservoirs. *Geochim. Cosmochim. Acta* **109**, 280–295.

Wasserburg G. J., Lee T. and Papanastassiou D. A. (1977) Correlated O and Mg isotopic anomalies in Allende inclusions. II – magnesium. *Geophys. Res. Lett.* **4**, 299–302.

Wood J. A. (1998) Meteoritic evidence for the infall of large interstellar dust aggregates during the formation of the solar system. *Astrophys. J.* **503**, L101–L104.

Zhang J., Huang S., Davis A. M., Dauphas N., Hashimoto A. and Jacobsen S. B. (2014) Calcium and titanium isotopic fractionations during evaporation. *Geochim. Cosmochim. Acta* **140**, 365–380.

Associate Editors: Alexander Krot, Yuri Amelin, Sara Russell and Qing-Zhu Yin